Geochimica et Cosmochimica Acta 363 (2023) 51–67

Contents lists available at ScienceDirect

Geochimica et Cosmochimica Acta

journal homepage: www.elsevier.com/locate/gca

Biogeochemistry of iron in coastal Antarctica: isotopic insights for external sources and biological uptake in the Amundsen Sea polynyas

Hung-An Tian [a,*], Mathijs van Manen [a], Zach B. Bunnell [b], Jinyoung Jung [c], Sang Hoon Lee [c], Tae-Wan Kim [c], Gert-Jan Reichart [a,d], Tim M. Conway [b], Rob Middag [a,e,*]

[a] NIOZ Royal Netherland Institute for Sea Research, Department of Ocean Systems, PO Box 59, 1790 AB Den Burg, the Netherlands
[b] College of Marine Science, University of South Florida, St Petersburg, FL 33701, USA
[c] Korea Polar Research Institute, 26, Songdomirae-ro, Yeonsu-gu, Incheon 21990, Republic of Korea
[d] Faculty of Geosciences, Utrecht University, 3584 CB Utrecht, the Netherlands
[e] Centre for Isotope Research – Oceans, University of Groningen, PO Box 72, 9700 AB Groningen, the Netherlands

ARTICLE INFO

Associate editor: Tristan J Horner

Keywords
GEOTRACES
Trace metals
Isotopic compositions
Biogeochemistry

ABSTRACT

Seasonal phytoplankton blooms in the Antarctic Amundsen Sea Polynyas are thought to be supported by an external supply of iron (Fe) from circumpolar deep waters, benthic sediments, and/or ice shelf meltwaters. However, largely due to the limited amount of Fe data reported for the Amundsen Sea Polynyas, understanding of the sources and processes that affect the biogeochemistry of Fe in this region (notably within the ice shelf system) remains limited. Here, we present the first investigation of dissolved Fe isotope distributions (δ^{56}Fe) along the conveyer belt of waters into and through the Amundsen Sea, via the Dotson Ice Shelf, from samples collected during austral summer (2017–2018). Our dataset allows us to characterize and compare the dissolved δ^{56}Fe signatures of incoming modified Circumpolar Deep Water (mCDW) and of sedimentary sources on the continental shelf. The range in dissolved δ^{56}Fe (–1 to +0.1 ‰) observed in the Amundsen Sea close to the seafloor, coupled with elevated dissolved Fe concentrations (up to 1.6 nmol/L), suggests that Fe is released from shelf sediments via a combination of reductive and non-reductive processes, with non-reductive dissolution input being relatively more important (20–56 %) than reductive dissolution (4–12 %). Near the Dotson Ice Shelf, the δ^{56}Fe in the mCDW inflow (–0.70 ‰) was lower than the mCDW outflow (–0.23 ‰), whereas any change in dissolved Fe concentrations was negligible. We speculate that this shift in dissolved δ^{56}Fe underneath the ice shelf is driven by a combination of enhanced preservation (and addition) of lithogenic colloidal Fe(III) and/or complexation with Fe-binding ligands, together with a differential loss of Fe^{2+}. We also found distinct δ^{56}Fe signatures in surface waters of the polynya, with apparent preferential uptake of isotopically light Fe in a bloom dominated by diatoms leading to a relatively heavy remnant dissolved δ^{56}Fe signature of +1.06 ‰, compared to a bloom dominated by haptophytes where more modest and variable isotope fractionation was observed. The different isotopic composition between the two regions could be related to the dominance of different species, but this remains speculative. Despite prominent biological uptake, we suggest that other factors such as rapid recycling (e.g., adsorption and regeneration), bacterial regeneration, and complexation with organic ligands, together with the supply of lithogenic particles also play important roles in setting surface dissolved δ^{56}Fe in the Amundsen Sea Polynyas. Overall, this study provides a further understanding of the external Fe sources and the biogeochemical processes in the Amundsen Sea and thus a baseline on how changing conditions in Antarctica can affect Fe cycling in the Southern Ocean and beyond.

1. Introduction

Iron (Fe) is an essential micronutrient participating in many important metabolic processes (e.g., nitrogen fixation and photosynthesis) for marine phytoplankton (e.g., Morel and Price, 2003). In the Southern Ocean, the largest high-nutrient low-chlorophyll region, the availability of Fe and the intensity of irradiation are generally the limiting factors for the growth of marine organisms (Boyd et al., 2007; de Baar et al., 1995;

* Corresponding authors.
E-mail addresses: hung-an.tian@nioz.nl (H.-A. Tian), rob.middag@nioz.nl (R. Middag).

https://doi.org/10.1016/j.gca.2023.10.029
Received 13 December 2022; Accepted 24 October 2023
Available online 28 October 2023

Martin et al., 1990). Pervasive Fe limitation over large regions of the surface Southern Ocean results from a combination of a limited supply of dissolved Fe (dFe) from upwelling deep waters compared to macronutrients, and very limited external Fe sources to the region (e.g., Tagliabue et al., 2014). However, in contrast to the open Southern Ocean, coastal polynyas – areas of reduced ice cover driven by offshore katabatic winds and/or the intrusion and subsequent upwelling of warm and saline Circumpolar Deep Water (CDW) (Jacobs et al., 2011; Jenkins et al., 2010; Vaughan, 2008; Wåhlin et al., 2010; Walker et al., 2007) – are observed to be seasonally highly productive, notably in austral spring and summer (Arrigo et al., 2008, 2012). The intrusion of CDW in the Amundsen Sea (AS) occurs on the continental shelf as CDW passes the continental shelf break and/or upwells via local Ekman pumping (e.g., Jacobs et al., 1996; Jenkins et al., 2010; Kim et al., 2021). Depending on the extent of mixing, CDW may be modified and is then described as modified CDW (mCDW) (Wåhlin et al., 2010). The inflowing mCDW subsequently flows underneath (and flows out from under) the Dotson Ice Shelf (DIS), causing significant basal melting of the ice shelf in the shelf cavity. Such upwelling of CDW accelerates the thinning, melting and subsequent collapse of Antarctic ice shelves that form drifting icebergs (Gourmelen et al., 2017; Jacobs et al., 2011; Rignot et al., 2008) and releases glacial/ice sheet-derived Fe to seawater (Klunder et al., 2011; Raiswell et al., 2006; Sedwick and DiTullio, 1997). Moreover, the reduction of ice cover in the polynya and consequent enhanced irradiation, in combination with an additional Fe supply, enables the formation of phytoplankton blooms in Antarctic coastal polynyas (Alderkamp et al., 2012; Arrigo et al., 2008), which are potentially responsible for a large proportion of carbon uptake in the Southern Ocean (Arrigo and van Dijken, 2003; Sarmiento et al., 2004). Amongst all the Antarctic polynyas, the Amundsen Sea Polynya (ASP), in which the rates of ice-sheet thinning are the highest of all Antarctica (Paolo et al., 2015; Rignot et al., 2019), exhibits the highest rate of annual net primary production per unit area (160 ± 37 g C/m^{-2} y^{-1}, Arrigo and van Dijken, 2003; Arrigo et al., 2008).

As the ASP is one of the most productive polynyas, understanding rapid changes in the ice sheet dynamics and biogeochemistry (e.g., Fe supply to coastal waters) is key to understanding how climate change impacts both the Antarctic ecosystem and elemental cycling in the Southern Ocean. However, due to the remoteness of Antarctica and limited accessibility underneath ice shelves, there was an absence of data on whether mCDW-induced melting serves as an additional Fe supply for spring/summer phytoplankton blooms in the ASP until the first investigation of dissolved Fe (dFe) at the Pine Island Glacier (Alderkamp et al., 2012; Gerringa et al., 2012, 2020b) and subsequent studies focusing on dFe and particulate Fe (pFe) in the CDW inflow and outflow at the Dotson Ice Shelf (DIS) (Planquette et al., 2013; Sherrell et al., 2015). Based on dFe and pFe concentrations, these investigations suggested that the inflowing mCDW, characterized as 'Fe-rich' deep water, with an addition of sedimentary Fe input and ice-shelf derived Fe, provides a continuous dissolved Fe supply fuelling phytoplankton blooms in the surface of the ASP via buoyancy-driven mixing ('the meltwater pump') underneath the ice shelf (Sherrell et al., 2015; St-Laurent et al., 2019). However, a recent study in the ASP argued instead that ice-shelf dFe is most likely negligible compared to sediment input and mCDW, based on a conservative mixing model (van Manen et al., 2022); that study also speculated that a fast equilibrium between dFe and labile pFe underneath the DIS moderated the concentrations of dFe in the mCDW outflow, as well as the amount of Fe supplied to the surface polynya via the 'meltwater pump'.

In the last 10–15 years, dissolved Fe isotope ratios (δ^{56}Fe) has provided considerable insight into the differing regional importance of external sources of Fe to the ocean, as well as enhancing understanding of the internal biogeochemical cycling processes that affect the distribution and cycling of Fe in the oceans (recently reviewed in detail by Fitzsimmons and Conway (2023)). The δ^{56}Fe endmember signatures of different external sources to the oceans are now reasonably well constrained, although uncertainties and caveats remain. For example, atmospheric desert dust is well characterized at +0.1 ‰ (Beard et al., 2003; Conway et al., 2019), while anthropogenic combustion and biomass burning aerosols may range from –4‰ to +0.3 ‰ (Conway et al., 2019; Kurisu et al., 2016a; Kurisu et al., 2021; Kurisu et al., 2016b). In sediments, different mechanisms lead to diverse sedimentary δ^{56}Fe signatures. For example, reductive dissolution (RD) leads to elevated concentrations of reduced Fe in porewater that can diffuse into bottom waters, where the size of the flux depends on the absence/presence (and thickness) of an overlying oxygenated surface sediment layer where Fe^{2+} can be oxidized prior to diffusion. However, likely due to differences in the intensity of reduction processes within sediments and oxidation of Fe in an oxygenated surface sediment layer or in near bottom seawater, reductive dissolution is characterized by a wide range of isotopically light signatures (–3.5 to –1‰, e.g., Homoky et al., 2021; Johnson et al., 2020; Severmann et al., 2006). Conversely, non-reductive dissolution (NRD) induced via particle and colloid weathering and ligand mediated dissolution, often facilitated by sediment resuspension, have been suggested to exhibit a relatively consistent isotopic signature (~+0.1 ‰, e.g., Homoky et al., 2013; Homoky et al., 2021; Radic et al., 2011) compared to RD. High temperature hydrothermal vent fluids are also fairly well constrained (–0.7 to –0.1 ‰), but chemical complications upon mixing with ocean waters lead to a wide range of vent-specific signatures (–4 to +0.5 ‰; e.g., Ellwood et al., 2015; Fitzsimmons et al., 2017; Lough et al., 2017; Wang et al., 2021). Rivers are perhaps the least well constrained (–1.3 to +1.8 ‰), with large variability in δ^{56}Fe between river types and locations highly dependent on chemical conditions such as colloidal concentration, pH, and mineral compositions (Dauphas et al., 2017; Fitzsimmons and Conway, 2023). Most relevant for this work, a limited number of studies suggests that dissolved δ^{56}Fe signatures of polar sources are often driven by biogeochemical processes rather than being representative of source material. For example, while dissolved δ^{56}Fe measured in Greenland glacier streams was close to crustal due to physical weathering (Schroth et al., 2011; Stevenson et al., 2017; Zhang et al., 2015), in Arctic subglacial streams dissolved δ^{56}Fe reached values as light as –2.1 ‰, attributed to silicate weathering, pyrite oxidation and dissimilatory Fe reduction from glacial sediments (Henkel et al., 2018; Stevenson et al., 2017). Dissolved δ^{56}Fe measured in arctic sea ice, meltwater ponds and snow has also been found to be isotopically light, due to photoreduction or biological activity (Marsay et al., 2018). In Antarctica, the saline Fe-rich 'Blood falls' from the Taylor Glacier had an δ^{56}Fe signature of –2.6 ± 0.5 ‰ (Mikucki et al., 2004), indicative of reductive dissolution of sediments. At the broader scale, recent polar Fe and δ^{56}Fe studies have implicated Antarctic and Arctic marginal processes in supplying isotopically light Fe from non-reductive dissolution to Arctic shelf environments and to Antarctic coastal and offshore waters (Sieber et al., 2021; Zhang et al., 2021), with evidence of long distance transport of Antarctic margin derived-Fe into the Southern Ocean and the South Atlantic (e.g., de Jong et al., 2012; Hatta et al., 2013; Klunder et al., 2014; Measures et al., 2013; Sieber et al., 2021). However, despite the obvious importance of the Southern Ocean to the global ocean and global climate, and the role of sedimentary margins in fuelling productivity in coastal Antarctica and beyond, there is still a paucity of dissolved δ^{56}Fe data from the Southern Ocean and coastal Antarctica, with only three studies published (Abadie et al., 2017; Ellwood et al., 2015; Sieber et al., 2021).

In addition to constraining external Fe sources, various processes including biological uptake (e.g., Ellwood et al., 2020; Ellwood et al., 2015), organic ligand complexation (e.g., Dideriksen et al., 2008; Ilina et al., 2013; Morgan et al., 2010), adsorption (e.g., Johnson et al., 2008; Mulholland et al., 2015), scavenging (e.g., Radic et al., 2011), regeneration (e.g., Abadie et al., 2017; Klar et al., 2018), and redox reactions of Fe species (e.g., Beard and Johnson, 2004; Ellwood et al., 2015) may fractionate Fe isotope ratios. In turn, δ^{56}Fe provides additional opportunities to disentangle a suite of processes that are not easily evaluated by [dFe] alone. For example, Ellwood et al. (2015) utilized δ^{56}Fe of dFe

and pFe during the development of a subtropical phytoplankton bloom to reveal how the dominant processes that influenced Fe cycling developed from photochemical (and biological) reduction at the onset of the bloom to biological uptake at the peak of the bloom. More recently, Sieber et al. (2021) used dissolved δ^{56}Fe to fingerprint the processes (e.g., biological uptake, recycling, and ligand binding) that dominated Fe cycling in surface waters across all major zones of the Southern Ocean. In the ASP, the interplay of multiple biogeochemical processes and long-lasting phytoplankton blooms provide an ideal opportunity to investigate δ^{56}Fe systematics.

Here, following a previous study on dissolved and particulate Fe concentrations in the ASP (samples collected during the same expedition as this study, van Manen et al., 2022), we present the first dataset of δ^{56}Fe from the Amundsen Sea (AS), from a transect following the inflowing mCDW and its passage through the AS and its outflow from the DIS. We use this dataset to build on the previous study and further evaluate the sources of sedimentary Fe and ice-shelf melt derived Fe, as well as to investigate the processes occurring underneath the DIS that determine the speciation and magnitude of Fe being released by the meltwater pump. Additionally, we characterize dissolved Fe isotopic signatures in ASP surface waters during two austral summer phytoplankton blooms dominated by two different phytoplankton communities (haptophytes and diatoms), specifically allowing us to study a combination of biological fractionations and physical processes that result in variable Fe isotope signatures in the surface waters of the polynyas.

2. Materials and methods

2.1. Sampling region and sampling for dissolved Fe

GEOTRACES process study (ID: GPpr12; expedition: ANA08B) was conducted on the Korean icebreaker R/V Araon in the AS during Austral Summer 2017/2018 (December 2017–February 2018). Seawater samples from two transects through the ASP presented in this study were collected between 24th January and 2nd February 2018. The first transect (24th–29th January) followed CDW intrusion from the Antarctic continental shelf break onto the continental shelf via the Dotson-Getz trough (modified to mCDW since it mixes with overlying shelf waters), the subsequent flow south-eastward into the cavity underneath

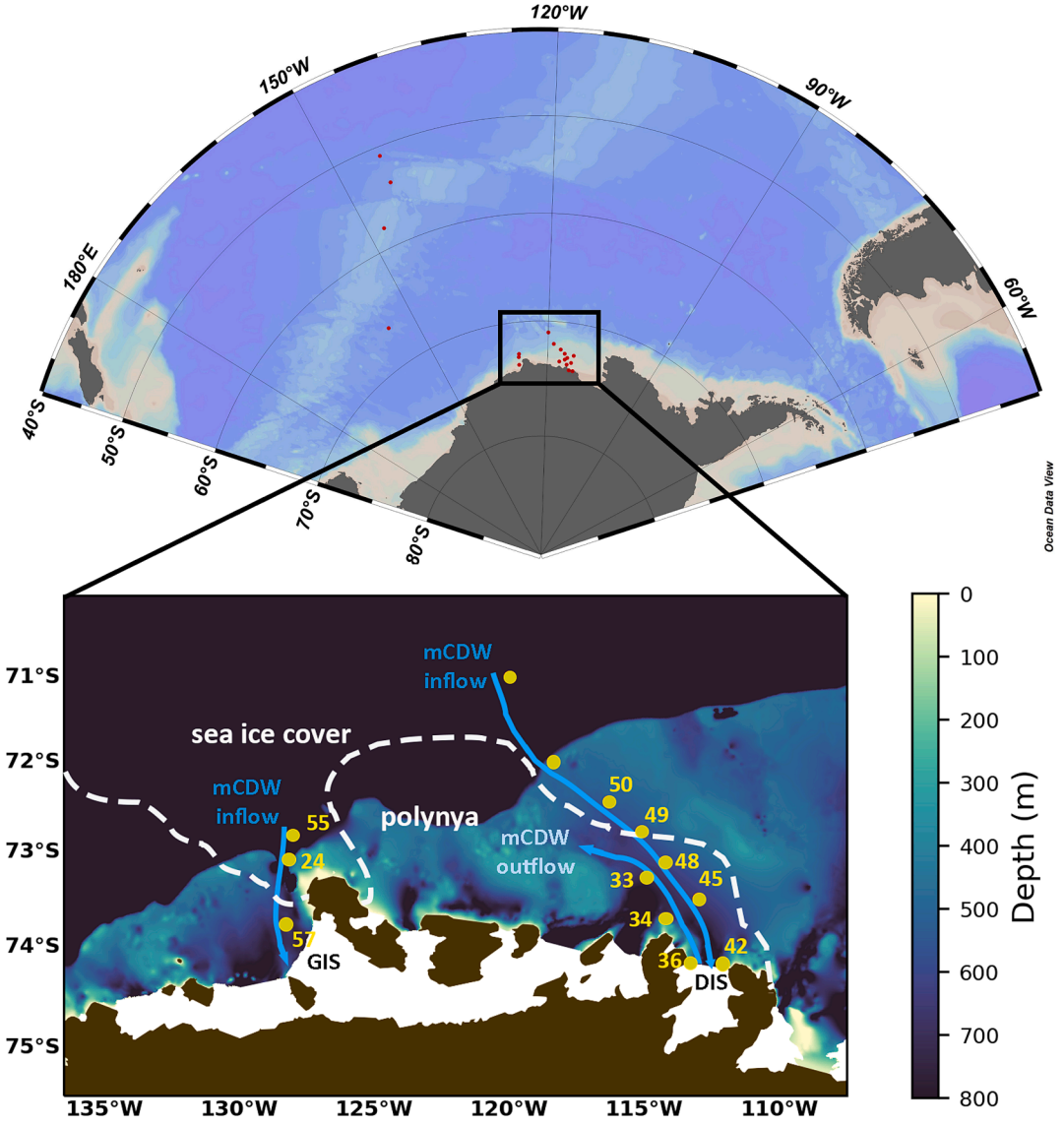

Fig. 1. GPpr12 sampling stations at the Dotson Ice Shelf (DIS) and Getz Ice Shelf (GIS) regions in the Amundsen Sea. Stations are grouped based on the direction of mCDW intrusion – the DIS(inflow) stations (Stn 50, 49, 48, 45, and 42), the $DIS_{(outflow)}$ stations (Stn 36, 34, and 33), and the $GIS_{(inflow)}$ stations (Stn 55, 24, and 57). The white dashed line indicates the sea ice cover during the sampling period.

the Dotson Ice Shelf (DIS), and then the later emergence at shallower depths from underneath the DIS. The second transect (1st–2nd February) followed mCDW inflow along Siple trough towards Getz Ice Shelf (GIS) (Fig. 1). Each station comprised 10–14 sampling depths from the near-surface (~10 m) to 1000 m, or 10–20 m above the seafloor for stations shallower than 1000 m. The stations located in the mCDW inflow (Stns 50, 49, 48, 45, and 42) and the mCDW outflow (Stns 36, 34, and 33) in the DIS region are henceforth referred to as the $DIS_{(inflow)}$ stations and the $DIS_{(outflow)}$ stations, respectively. Additionally, seawater samples were also collected at three stations in GIS region (referred to as the $GIS_{(inflow)}$ stations: Stns 55, 24, and 57) along the mCDW inflow (Fig. 1).

The sampling procedure for dissolved metals was as previously reported by van Manen et al. (2022). Briefly, samples for dissolved Fe isotope analysis were collected using the Royal Netherlands Institute for Sea Research (NIOZ) "Titan" ultra-clean sampling system for trace metals (de Baar et al., 2008; Rijkenberg et al., 2015), equipped with multiple auxiliary sensors for basic parameters (e.g., salinity, temperature, and fluorescence). Subsequently, seawater samples were filtered through 0.2 μm filter cartridge (Sartobran-300, Sartorius, precleaned with MQ water, 18.2 MΩ cm^{-1}) into 4 L LDPE cubitainers (for surface samples) and 1 L LDPE bottles. All containers used in the sampling were precleaned following GEOTRACES cookbook (version 3.0, 2017) and Middag et al. (2019). The filtered samples were then acidified to 0.024 M HCl using 12 M ultrapure concentrated HCl (Baseline, Seastar Chemicals Inc.), resulting in a final pH of ~1.8. Acidified samples were stored at room temperature for over five months before processing for isotope ratios at NIOZ.

Table 1
Extraction and purification procedure implemented in this study, modified from Conway et al. (2013).

Extraction	
1.	Preclean Nobias PA-1 resin with 4 mL 3 M HNO_3
2.	Precondition resin with 4 mL diluted buffer (ammonia acetate, pH = 6.5) (MQ: buffer = 5:1)
3.	Adjust pH in samples to 4.5 ± 0.05 with concentrated buffer (ammonia acetate, pH = 6.5)
4.	Pass samples through resin by gravity with a duration less than 12 h
5.	Rinse resin with 3 changes of 15 mL MQ
6.	Elute metals with 8 mL 3 M HNO_3
7.	Evaporate samples at 180°C. Reconstitute and reflux samples in 3 mL of concentrated HNO_3 and 10 % H_2O_2 to dissolve organics for 2 h
8.	Evaporate samples at 180°C. Reconstitute and reflux samples in 200 μL of 7 M HCl + 0.001 % H_2O_2 for purification
Purification	
1.	Load 30 μL precleaned AG-MP 1 resin to microcolumns
2.	Clean microcolumns (with resin loaded) with 2 × 250 μL 7 M HCl + 0.001 % H_2O_2
3.	Rinse resin with 4 × 60 μL MQ
4.	Precondition columns with 200 μL 7 M HCl + 0.001 % H_2O_2
5.	Add samples
6.	Elute salts, Cu, Ni, Pb, and Co with 16 × 30 μL 7 M HCl + 0.001 % H_2O_2
7.	Elute Fe with 10 × 30 μL 1 M HCl.
8.	Elute Zn with 10 × 30 μL 2 M HNO_3 + 0.1 M HBr
9.	Elute Cd with 10 × 30 μL 2 M HNO_3
10.	Evaporate samples at 180°C. Reconstitute and reflux samples in 3 mL of concentrated HNO_3 and 10 % H_2O_2 to dissolve organics for 2 h
11.	Evaporate samples at 180°C. Reconstitute in 0.1 M HNO_3 for MC-ICPMS analysis

2.2. Analytical methods for Fe isotopes

Initial chemical processing of samples took place at NIOZ, with subsequent purification and analysis at the University of South Florida (USF). Dissolved Fe isotope ratios were measured by Thermo Neptune multi-collector ICPMS (MC-ICPMS) using a double spike analytical technique modified from Conway et al. (2013). Sample processing for Fe isotope analysis was carried out in the clean room at NIOZ (ISO class 7, ISO class 5 in working hoods), or in an ISO class 6 clean laboratory at USF. All containers and components used for chemical analysis were precleaned following GEOTRACES cookbook (version 3.0, 2017) and Middag et al. (2019), and all reagents were double distilled from VWR NORMAPUR (NIOZ) or Fisher Scientific Trace Metal Grade (USF) by PFA Savillex Stills prior used for analysis. Acidified seawater samples were spiked with a ^{57}Fe-^{58}Fe double spike at least 48 h prior to further treatment (extraction and purification) with a sample-to-spike ratio of 1:2 (nmol L^{-1}: nmol L^{-1}) (Sieber et al., 2021), guided by sample dFe concentrations measured independently by a SeaFAST system and Element 2 ICPMS as reported previously (van Manen et al., 2022).

2.2.1. Extraction and purification

An extraction and purification procedure for Fe from seawater was based on Conway et al. (2013) and was modified at NIOZ. The extraction procedure is shown in Table 1; for exaction, polypropylene tubes with polyethylene frits fitted to the bottom of the tubes were attached under separatory FEP funnels (Thermo Scientific™ Nalgene™, volume: 1 and 2 L). The tubes were filled with Nobias PA-1 chelating resin (~2 mL) and rinsed with MQ (15 mL, repeat three times) prior to loading samples. The pH values of samples were adjusted to 4.5 ± 0.05 using ammonia acetate (pH = 6.5) before eluted with 8 mL 3 M HCl (Table 1). After processing each sample, funnels and tubes (with resins loaded) were cleaned with 3 M HNO_3 and samples were then purified using LDPE microcolumns (with polyethylene frits) loaded with 30 μL Biorad™ AGMP-1 resin to separate Fe from interfering elements (the purification procedure is shown in Table 1). After processing each sample, AGMP-1 resin was discarded and the microcolumns (with frits) were cleaned in 1 M HCl at 60°C. The samples (0.5–1 mL) were shipped to USF for Fe isotope analyses in 8 mL LDPE bottles (Nalgene) that are routinely used for trace metal sampling. Samples were then re-purified using AGMP-1 microcolumns at USF (Sieber et al., 2021) prior to MC-ICPMS analysis. This second purification at USF was to ensure complete removal of Ca and Na from samples, as these elements can cause inaccuracy in Fe isotope analysis (Lacan et al. (2021) and our in-house experience).

An estimation of the procedural blank for the method was determined by processing acidified ultrapure water through the full method described in Table 1. The extraction blank was 0.38 ± 0.08 ng (n = 11), the NIOZ purification blank was 0.15 ± 0.09 ng (n = 6), and the USF second purification blank was 0.13 ± 0.15 ng (n = 5). The total blank value (~0.66 ng per sample) is generally two orders of magnitude lower than natural Fe in our samples after the pretreatment, as well as being too small to measure the blank isotopic composition; as such we follow Sieber et al. (2021) and do not apply blank corrections to dFe or $\delta^{56}Fe$.

2.2.2. Measurements of Multi-Collector ICPMS (MC-ICPMS)

Fe isotope analysis was carried out using a double-spike technique on a Thermo Neptune Plus MC-ICPMS in the Tampa Bay Plasma Facility at USF. The details of the instrumental settings, including introduction system, cones, cup configuration, mass bias correction, and double spike technique performance, are identical to those described by Sieber et al. (2021). Here, we express Fe isotope ratios in typical delta notations relative to the IRMM-014 standard:

$$\delta^{56}Fe\,(‰) = \left[\frac{\left(^{56}Fe/^{54}Fe\right)_{sample}}{\left(^{56}Fe/^{54}Fe\right)_{IRMM-014}} - 1\right] \times 1000$$

External precision at USF is approximated by the long-term instrumental precision on the secondary NIST SRM 3126a, with a value of +0.36 ± 0.05 ‰ (mean ± 2SD, n = 524) obtained over 37 sessions (Hunt et al., 2022), which agrees with literature values (Conway et al., 2013; +0.35 ± 0.08 ‰; +0.39 ± 0.13 ‰, Rouxel and Auro, 2010; +0.32 ± 0.02 ‰, Sun et al., 2021). We thus consider 0.05 ‰ to be a conservative estimate of uncertainty and apply this to all samples, except for those where the 2 SE of an individual analysis is larger, in which case we

use this as a measure of uncertainty. The accuracy of the modified extraction and purification procedure was also tested by doping the same secondary Fe standard (NIST-3126) into acidified MQ that was processed as a sample and measured alongside natural samples. The average δ^{56}Fe of +0.35 ± 0.02 ‰ (2 SD, n = 3) of this test agrees with the expected value.

Uncertainty on Fe concentrations using this method is typically assumed to be 2 % (Conway et al., 2013), and the accuracy of this method has been demonstrated previously (Conway et al., 2016; Conway et al., 2013). Further, dFe concentrations derived from the isotope dilution technique after measurement using the Neptune Plus MC-ICPMS agreed well with dFe concentration obtained from the SeaFAST based measurements on the Element 2 ICPMS (Supplementary Fig. S1; van Manen et al., 2022). In this study, since there is good agreement between the two methods for dFe in most samples, we use the mean dFe concentration calculated for each sample from the two methods.

2.2.3. Production of figures

For the figures used in this study, Ocean Data View (ODV version 5.3.0, Schlitzer, 2020) was used to produce Fig. 1 (top figure), Figs. 2, 3 and 6b. SigmaPlot (version 14) was used to produce Figs. 4, 5, 6a and 7. Fig. 8 was generated using Microsoft PowerPoint. Fig. 1 (bottom panel) was generated using Python (version 3.7.12). The calculation of the double spike deconvolution was performed using an in-house Microsoft Excel Macro based on the iteration principles published by Siebert et al. (2001).

3. Results

3.1. Oceanographic setting

In the AS, three water masses – Antarctic Surface Water (AASW), Winter Water (WW), and CDW (and mCDW) – are typically observed during austral summer (Randall-Goodwin. et al., 2015; Yager et al., 2012) and were observed during this expedition (Fig. 2). AASW is a result of enhanced solar irradiation and associated sea ice melt in summer, with conservative temperature (Θ) from –0.6 to –0.7 °C and absolute salinity (S_A) less than 33.8. AASW was observed in the upper 40 m at the $DIS_{(inflow)}$ stations and $DIS_{(outflow)}$ stations (Fig. 3a); whereas it was not clearly observed in the surface waters of the $GIS_{(inflow)}$ stations (Fig. 3d). WW, located below AASW, is a remnant from the winter season due to brine rejection and cooling of surface water, with an Θ minimum (~–1.8 °C) and S_A from 34.3 to 34.4 (Fig. 3). As CDW (i.e., off-shelf waters before intruding onto the continental shelf) mixes with overlying WW, it is modified from the off-shelf endmember to form mCDW, with Θ ranging from –0.5 to 1.5 °C and S_A higher than 34.7 (Figs. 2 and 3).

3.2. Chlorophyll a fluorescence

Chlorophyll *a* fluorescence was relatively elevated in the upper 100 m of most $DIS_{(inflow)}$ stations and $DIS_{(outflow)}$ stations and in the upper 40 m of all $GIS_{(inflow)}$ stations (Fig. 3c and f), except one $DIS_{(outflow)}$ station (Stn 36) where fluorescence is relatively low compared to other stations. From here on, we define the surface layer as the water column between the surface and the depth where maximum fluorescence was observed; the fluorescence signal declined rapidly below this surface maximum (mostly within upper 200 m). The stations with elevated fluorescence are referred to as phytoplankton bloom stations (DIS bloom: Stns 33, 34, 42, 45, 48, 49, and 50; GIS bloom: Stns 24, 55, and 57) in this study as they have high chlorophyll *a* standing stock. These observations agree broadly with previous observations of annual phytoplankton blooms in the ASP (Alderkamp et al., 2015; Arrigo et al., 2012; Gerringa et al., 2012, 2020b; Yager et al., 2012).

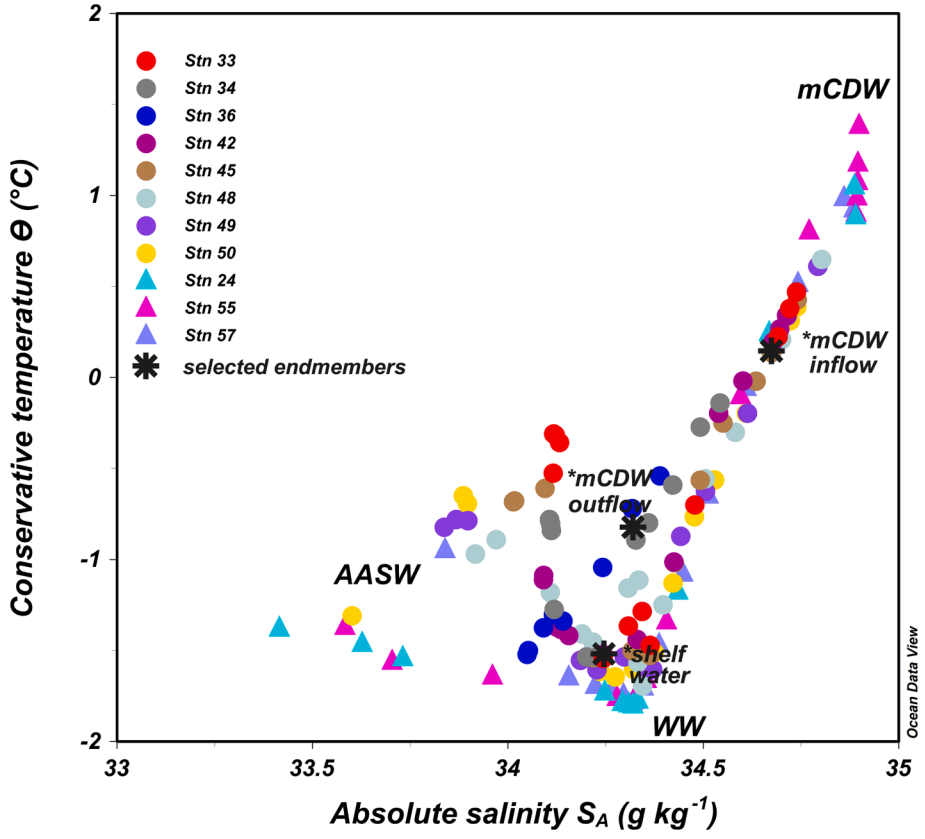

Fig. 2. Conservative temperature (Θ)-absolute salinity (SA) diagram. Three water masses are identified – Antarctic Surface Water (AASW), Winter Water (WW), and modified Circumpolar Deep Water (mCDW). The star signs represent the selected members used for conservative mixing discussed in Section 4.2.1.

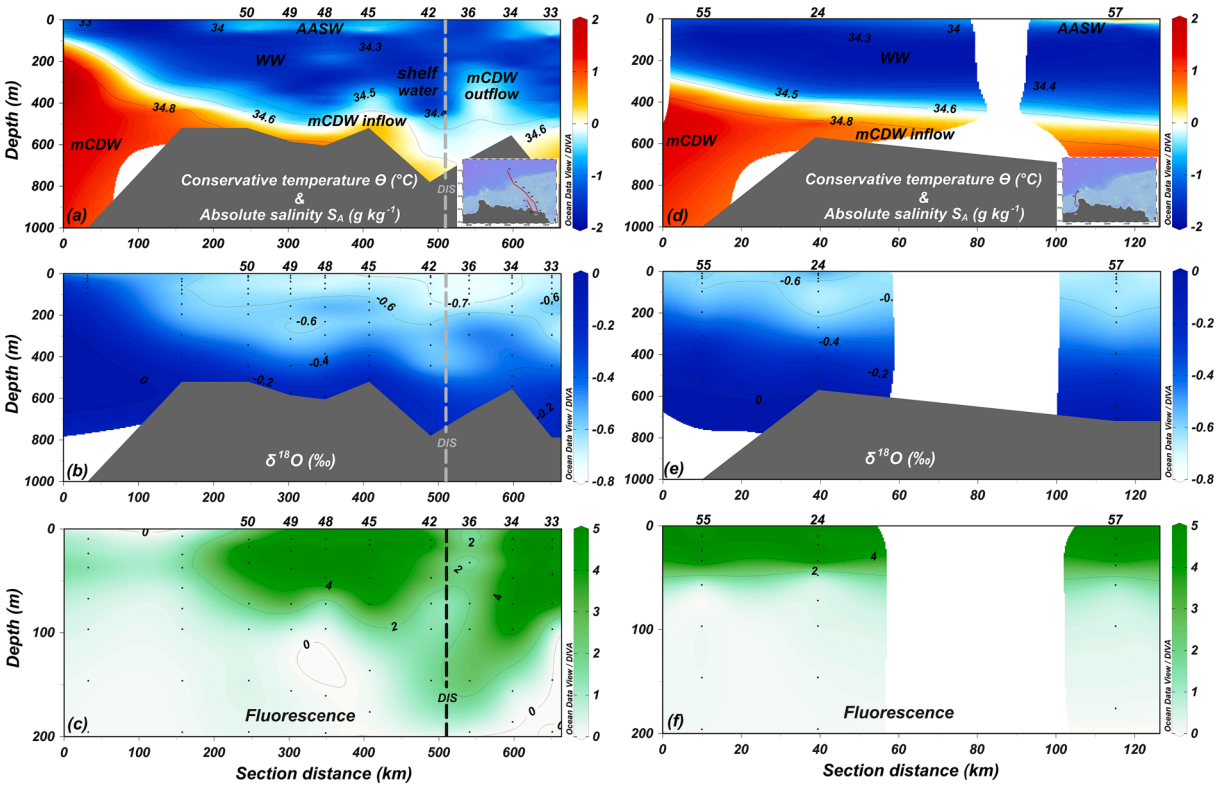

Fig. 3. Sections of conservative temperature Θ, absolute salinity (SA), and fluorescence of all GPpr12 stations included in this study. (a) to (c) the DIS(inflow) stations and the DIS(outflow) stations; (d) to (f) the GIS(inflow) stations. Note that (c) and (f) only show the upper 200 m of fluorescence.

3.3. Dissolved δ^{56}Fe and [dFe]

In the surface layer, dissolved Fe concentrations ([dFe]) were generally low at all stations – the $DIS_{(inflow)}$ stations (average: 0.25 nmol/L, ranging from 0.12 to 0.59 nmol/L); the $DIS_{(outflow)}$ stations (average: 0.14 nmol/L, ranging from 0.03 to 0.26 nmol/L); and the $GIS_{(inflow)}$ stations (average: 0.18 nmol/L, ranging from 0.08 to 0.26 nmol/L) (Fig. 4). On average, dissolved δ^{56}Fe exhibited elevated values in the $GIS_{(inflow)}$ stations (mean: +0.58 ‰, ranging from + 0.22 to +1.06 ‰), and lower (near to crustal values) in both the $DIS_{(inflow)}$ stations (mean: +0.10 ‰, ranging from –0.23 to +0.68 ‰) and the $DIS_{(outflow)}$ stations (mean: –0.03 ‰, ranging from –0.23 to +0.21 ‰) (Fig. 4). Between 200 and 400 m in the $DIS_{(outflow)}$ stations, [dFe] was elevated compared to the surface layer, with an average of 0.46 nmol/L that ranged from 0.29 to 0.66 nmol/L (the highest at Stn 36) (Fig. 4), which was lower than [dFe] in the core of mCDW inflow (Stns 45 and 42, 400–750 m) (Fig. 4). In terms of δ^{56}Fe, it was generally lower than that of the surface layer, ranging from –0.36 to +0.01 ‰ with a mean of –0.19 ‰ (Fig. 4).

Within 200 m above the seafloor, [dFe] increased at all stations compared to the water column above. In particular, elevated [dFe] was observed at depth in the $DIS_{(inflow)}$ stations (average: 0.76 nmol/L, ranging from 0.41 to 1.63 nmol/L) and the $DIS_{(outflow)}$ stations (average: 1 nmol/L, ranging from 0.57 to 2.03 nmol/L) with only relatively modest near-bottom elevations at the $GIS_{(inflow)}$ stations (average: 0.48 nmol/L, ranging from 0.39 to 0.64 nmol/L) (Fig. 4). For δ^{56}Fe, light Fe signals were observed close to the seafloor, with an average of –0.33 ‰ (ranging from –0.97 to +0.1 ‰), –0.56 ‰ (ranging from –1.08 to –0.24 ‰), and –0.11 ‰ (ranging from –0.25 to +0.08 ‰), for the $DIS_{(inflow)}$ stations, the $DIS_{(outflow)}$ stations, and the $GIS_{(inflow)}$ stations, respectively (Fig. 4). Stns 36 and 55 are excluded from the discussion below on sedimentary input as the bottom is much deeper than the Titan sampling system could reach due to the limited length of the cable used (Stn 55) and a malfunction of the system (Stn 36) respectively.

4. Discussion

In this study, we use the first dataset of dissolved δ^{56}Fe from the AS to investigate the varying importance of the external sources of dFe and the processes that control the biogeochemistry of dFe in the ASP. First, we discuss the importance of benthic sedimentary input, identifying the likely sedimentary release mechanisms (non-reductive vs reductive dissolution), and quantifying their relative contributions to the dFe pool. Second, we investigate the effect of potential processes occurring in the cavity under the DIS on dFe and δ^{56}Fe in the outflow, and discuss the hypothesis that relatively low [dFe] in the outflow is due to conservative mixing of the inflow with low dFe waters that are adjacent to the ice shelf, and dissolved-particle interactions (van Manen et al., 2022). Finally, we explore the isotopic fractionation of dFe in two different phytoplankton blooms, dominated by haptophytes and diatoms, and thus provide insights into the dynamics of Fe isotope composition in productive Antarctic coastal polynyas.

4.1. Benthic shelf sediments and CDW as dFe sources to the AS

Before intruding onto the continental shelf and transforming into mCDW, CDW exhibits relatively elevated [dFe] compared to surface waters (0.2–0.4 nmol/L, Sedwick et al., 2008; Sieber et al., 2021; Tagliabue et al., 2012; van Manen et al., 2022). Previously, it was estimated that incoming mCDW and benthic sediments contributed roughly equal amounts to the observed [dFe] (0.38 nmol/L and 0.33 nmol/L, respectively) in the mCDW near the DIS (van Manen et al., 2022), based on the distribution of dFe. However, with merely [dFe] it is difficult to distinguish different sources and processes as both RD and NRD could lead to release of dFe to bottom waters. Hence, while benthic sediments have previously been confirmed as an important Fe source in the AS, the dominant release mechanisms for sedimentary dFe input into the AS remain unknown. Here, we use dissolved δ^{56}Fe measurements in mCDW along the flow path into the AS to identify the different sedimentary

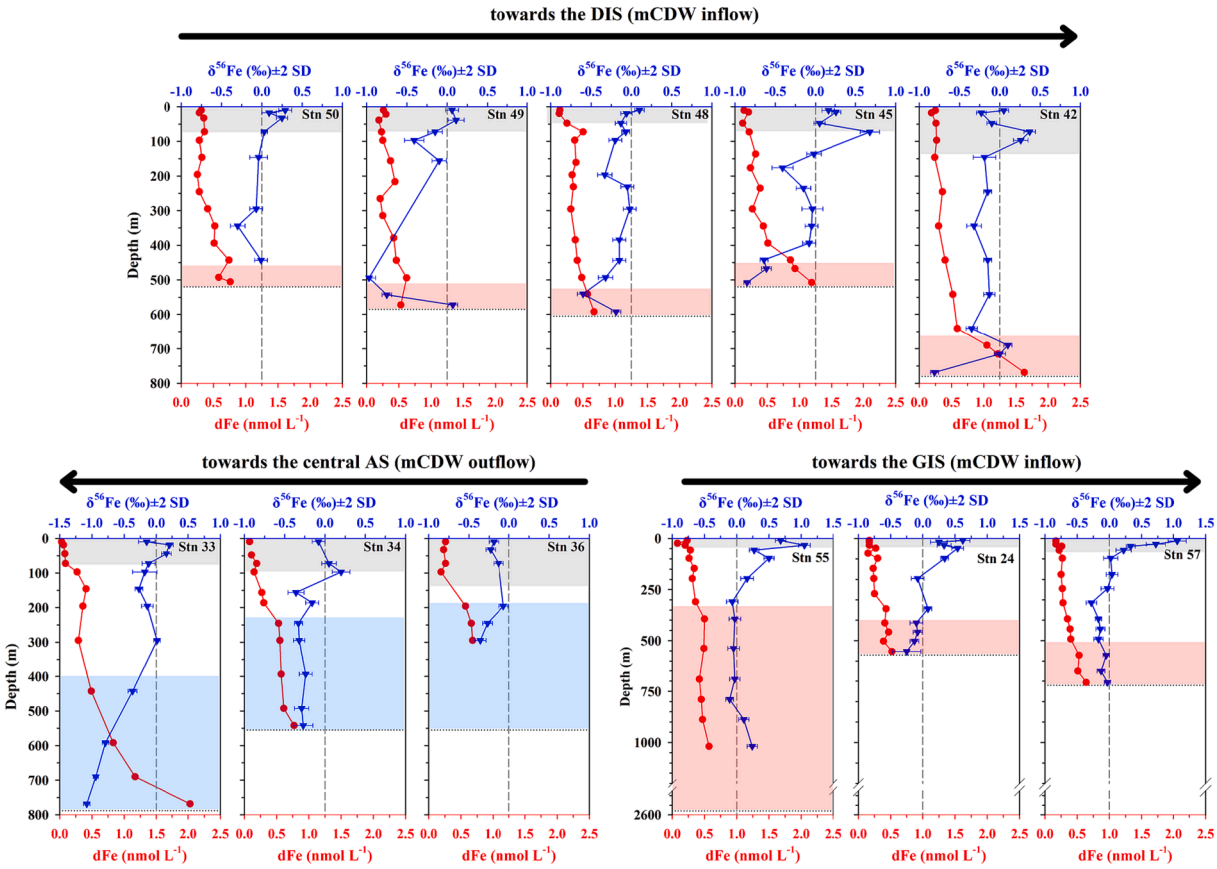

Fig. 4. Vertical water column profiles of dissolved Fe concentration ([dFe]) and δ56Fe from GPpr12 stations. dFe (red dots) corresponds to the bottom x-axis; whereas δ^{56}Fe (blue dots) corresponds to the top x-axis (error bar show two standard deviation (SD) for most samples, for samples that have 2 standard error lower than the long-term 2 SD of the internal standard – NIST SRM 3126a (+0.36 ± 0.05 ‰, n = 524), 0.05 is assigned as 2 SD). The grey dashed line indicates 0 ‰ of δ^{56}Fe, whereas the black dotted line indicates the bottom depth. The grey shading marks the surface layer (surface to fluorescence maximum depth); whereas the red and blue bars mark the depth of the mCDW inflow and outflow, respectively.

input sources of dFe (RD-dFe and NRD-dFe) and present a first attempt to quantify their relative contributions to mCDW in this region. As the core of mCDW inflow was located within 200 m above the seafloor (relatively well oxygenated with dissolved oxygen concentrations of 193–228 mol/L) in our dataset (van Manen et al., 2022), we only include samples in this depth range in our discussion.

4.1.1. *Constraining RD and NRD contributions to mCDW using δ^{56}Fe*

Within 200 m above the seafloor at the $DIS_{(inflow)}$ stations, δ^{56}Fe ranged from +0.10 to –0.97 ‰ with values becoming lower from offshore towards the DIS, while [dFe] increased from 0.41 nmol/L to 1.63 nmol/L (Fig. 4, Section 3.3). Both of these findings provide clear evidence for Fe addition from benthic sediments as mCDW travels towards the DIS. Likewise, at $GIS_{(inflow)}$ stations (Stns 24 and 57), low δ^{56}Fe (down to –0.25 ‰) with elevated [dFe] (up to 0.64 nmol/L) was observed close to the seafloor near the ice shelf (Fig. 4). In both cases, these isotopically light Fe signatures linked to elevated [dFe] are diagnostic of an input of dFe from RD (e.g., Homoky et al., 2009; John et al., 2012; Severmann et al., 2006; Severmann et al., 2010). Previously, elevated [Fe^{2+}] (e.g., RD derived) was observed in porewater samples collected in the AS, where a shallow oxygen penetration depth of only 1.8–3.6 cm (Kim et al., 2016) can enable diffusion of Fe^{2+} from porewaters into bottom water. Typically, RD-derived dFe initially ranges from −2 to −1.5 ‰; but the values can become even lower following precipitation of relatively heavy Fe(III) oxyhydroxides (typically ≥ −3.5 ‰) (Crosby et al., 2007; Fitzsimmons and Conway, 2023; Homoky et al., 2009; Severmann et al., 2010). To date, a range of endmember δ^{56}Fe compositions have been previously reported or assumed for the signature of the benthic flux of Fe derived from RD into bottom waters (–3.5 to –0.93 ‰ as summarised by Johnson et al. (2020) and Fitzsimmons and Conway (2023)), with variability likely dependent on sediment and bottom water conditions (e.g., redox cycles in porewater particulates).

Previously, the proportion of dFe in mCDW to dFe in sediment was estimated to be 1.2:1 (0.38:0.31 nmol/L) based on concentration data and the assumption that there were no other sources involved at the same depth along the DIS inflow transect (van Manen et al., 2022). If RD was the main sedimentary process supplying dFe to the mCDW inflow, then the expected dissolved δ^{56}Fe in the outflow should range from –1.6 to –0.4, based on the roughly equal proportions of dFe in the mCDW to dFe in sediment (1.2:1) and assuming similar δ^{56}Fe as previously reported elsewhere for RD fluxes to bottom waters (–3.5 to –0.93 ‰) and a mCDW signature of ~0 ‰ (Sieber et al., 2021) (see also Section 4.1.2). However, while this range overlaps with our observations near the DIS, some of our samples are notably heavier (up to +0.1 ‰, suggesting an additional heavier dFe source (e.g., NRD) other than CDW and RD. Previously, a near-crustal δ^{56}Fe value for NRD (+0.2 ± 0.2 ‰) was reported for porewater samples collected from the Cape margin (South Africa), a passive-tectonic and semi-arid ocean margin (Homoky et al., 2013; Homoky et al., 2009), as well as from seawater near the Papua New Guinea coast (Radic et al., 2011). Most recently, the signature of NRD was more tightly constrained at +0.07 ± 0.07 ‰ based on lithogenic colloidal Fe in porewaters collected from across the Southwest Atlantic Ocean (Homoky et al., 2021). Such lithogenic colloidal Fe has been suggested to result from physical weathering of sediments, which is more likely decoupled from organic matter content and oxygen

concentrations, in contrast to RD, and has potential to enable long term transport of Fe after it leaves the sediments (e.g., Conway and John, 2014; Homoky et al., 2021; Jensen et al., 2020).

Therefore, although there are no direct porewater δ^{56}Fe measurements in the AS, we note that, with higher δ^{56}Fe compared to RD endmembers, NRD (~+0 ‰) likely contributes isotopically-heavier crustal dFe to the mCDW, explaining the higher δ^{56}Fe signal than expected based solely on a binary mixture of background CDW and RD. Using a simple mixing model based on both concentrations and isotopic composition, we are thus able to estimate the relative contributions of these three sources.

4.1.2. Relative contribution of dFe from CDW, RD and NRD

Using the combination of δ^{56}Fe and [dFe] within 200 m above the seafloor, we identified sedimentary dFe input from two different processes (Section 4.1.1). Here, we use a simple two-component isotope mixing model to estimate the relative contribution of RD and NRD for the samples collected within 200 m above the seafloor at the DIS$_{(inflow)}$ stations, assuming negligible isotope fractionation following addition to the water column. This assumption is consistent with a growing range of studies which suggest that the characteristically isotopically light Fe signatures from RD can persist in oxygenated ocean waters (e.g., Hunt et al., 2022; Severmann et al., 2010). The mixing model is described using the following equations:

$$dFe_{observed} = dFe_{CDW} + dFe_{sediment} \quad (1)$$

$$f_{CDW} + f_{sediment} = 1 \quad (2)$$

$$f_{sediment} = f_{RD} + f_{NRD} \quad (3)$$

$$\delta^{56}Fe_{sediment} = \delta^{56}Fe_{observed} - \delta^{56}Fe_{CDW} = f_{RD} \times \delta^{56}Fe_{RD} + f_{NRD} \times \delta^{56}Fe_{NRD} \quad (4)$$

where dFe, f, and $\delta^{56}Fe$ denote the dissolved Fe concentration, fraction, and Fe isotopic signature, respectively. To derive $dFe_{sediment}$, dFe_{CDW} was taken from van Manen et al. (2022) (0.38 nmol/L) where the least modified CDW was observed in the AS but located distant from the continental shelf (Stns 52 and 53, which were not measured for their Fe isotopic composition). To derive f_{RD} and f_{NRD}, an endmember estimate for $\delta^{56}Fe_{NRD}$ of +0.1 ‰ (Homoky et al., 2021) was used. For $\delta^{56}Fe_{RD}$, since a wide range has been reported (–3.5 to –0.93 ‰), we chose the minimum (–3.5 ‰), the maximum (–0.93 ‰), and the mean of the two extremes (–2.2 ‰), to account for uncertainty in the anticipated $\delta^{56}Fe_{RD}$ benthic flux endmember. For $\delta^{56}Fe_{CDW}$, the endmember (0 ‰) was taken from Sieber et al. (2021) observed in the upper CDW in the Southern Ocean, as no unmodified CDW was measured for δ^{56}Fe in this study. Consequently, the relative contribution of each of the three components – CDW-dFe (f_{CDW}), RD-dFe (f_{RD}), and NRD-dFe (f_{NRD}) – was estimated for two depth intervals of (1) within 200 m above the seafloor; and (2) within 100 m above the seafloor.

The results of this calculation are shown in Fig. 5 and Supplementary Table S1. Generally, f_{NRD} was higher than f_{RD}, with relatively small uncertainty (color shadings in Fig. 5) in f_{NRD} at most stations, except a large uncertainty in both f_{NRD} and f_{RD} at Stn 45 within 100 m above the seafloor when applying the minimum $\delta^{56}Fe_{RD}$ and maximum $\delta^{56}Fe_{RD}$ (Fig. 5b). This overall limited variability in f_{NRD} indicates that the choice of $\delta^{56}Fe_{RD}$ endmembers does not significantly affect our estimation of f_{NRD}. This finding is helpful because it means that any possible fractionation of the RD isotope endmember by removal processes within bottom waters would not change our conclusions. Therefore, we use the mean $\delta^{56}Fe_{RD}$ of the two extreme endmembers of the reported ranges (–2.2 ‰) as the general endmember for RD for the following discussion. Notably, this value is similar to that used previously by Conway and John (2014), who chose –2.40 ‰ to best represent reductive sedimentary endmember, based on modelled RD Fe fluxes from the San Pedro basin (John et al., 2012).

At the DIS$_{(inflow)}$ stations, f_{CDW} within 200 m of the seafloor ranged from 38 to 76 %, generally decreasing from the open ocean towards the DIS; meanwhile, f_{NRD} increased from 20 to 56 % while f_{RD} remained relatively stable (4–12 %) (Fig. 5a, Supplementary Table S1). Since sediment resuspension is considered to be an important release pathway for NRD-dFe colloids (Homoky et al., 2021), our calculated higher f_{NRD} than f_{RD} at these stations suggests resuspension is important for supplying dFe to bottom waters, linked to the turbulent flow of mCDW. Such resuspension would bring both RD-dFe (e.g., porewater reduced Fe^{2+}, Kim et al., 2016) into the overlying water as well as NRD-dFe, contributing more dFe than simple diffusion of Fe by RD from the sediment pore waters. In fact, f_{NRD} was highest at Stn 42 (up to 56 %, higher than both f_{CDW} and f_{RD}, Fig. 5a), suggesting accumulation of colloidal phase NRD-dFe in the inflow as it travelled towards the coast, and/or terrestrial input of lithogenic colloids from the Antarctic shore (van Manen et al., 2022). This finding, from an isotopic perspective, also corroborates the previous idea that particle resuspension from benthic sediment influences the magnitude and distribution of [dFe] in the AS (Sherrell et al., 2015). Alternatively, spatial and temporal heterogeneity of sediment conditions can also result in the difference in f_{NRD} and f_{RD}, assuming dFe derived from CDW stays constant during the course of inflow transport: more reducing sediment or thinner oxygenated surface layers may lead to more RD-dFe in porewater (e.g., Henkel et al., 2018), whereas more oxygenated sediments may result in relatively higher colloidal NRD-dFe in porewaters (e.g., Homoky et al., 2021). Indeed, δ^{56}Fe exhibits heterogeneity in the bottom-most samples along the DIS$_{(inflow)}$ stations (Fig. 4), suggesting both the flux and mechanism of supply of dFe varies geographically within the AS. However, as sediment samples were not collected during the ANA08B expedition and the composition of sediments was not determined, we cannot determine whether spatial heterogeneity or simultaneous release of both RD and NRD is the main driver of the observed isotopic signatures.

When investigating closer to the seafloor in the AS, and comparing samples from within 100 m to within 200 m from the seafloor (see above), a similar increasing trend in each sediment-derived fraction and [dFe] towards the DIS is observed (Fig. 5b); however, f_{NRD}, f_{RD}, and total [dFe] (i.e., sum of CDW-dFe, NRD-dFe, and RD-dFe) are all greater within 100 m compared to within 200 m above the seafloor (Supplementary Table S1), indicating that benthic sediment input has a greater effect on dFe closer to the sediments, linked to the core of mCDW being situated close to the bottom, while dFe may be lost due to removal (e.g., particle scavenging) or dilution (i.e., conservative mixing) further above the seafloor.

The relationship between [dFe] and absolute salinity (S_A) within 100 m (and 200–300 m) above the seafloor provides insights for assessing the role of conservative mixing – at stations distant from the DIS (Stns 50, 49, and 48) (Fig. 6a), the relationship follows a mixing line which indicates that physical mixing and dilution drive reduction of dFe away from the source, whereas close to the DIS (Stns 42 and 45), a sudden increase of dFe (up to 1.6 nM) at high salinity indicates a prominent addition of dFe, compared to Stns 50, 49, and 48 (Fig. 6a), accompanied by lower δ^{56}Fe values observed close to the seafloor at Stns 42 and 45 (down to –0.85 ‰) than at Stns 50, 49, and 48 (Fig. 4). A strong correlation ($R^2 = 0.822$, $p < 0.05$, excluding one sample at 689 m at Stn 42) between the fractions of RD-dFe and NRD-dFe indicates simultaneous addition of dFe from both sources (Fig. 6b), lending weight to the idea that sediment resuspension is important, as Fe derived from the two sources are thought to be present in different forms and sediment disturbance – not just simple diffusion from pore waters – is needed to release both at once (dFe^{2+} vs colloidal Fe(III), Homoky et al., 2013; Homoky et al., 2009; Homoky et al., 2021).

4.2. Biogeochemical processes under the DIS

Due to global warming, ice shelves and glaciers located near the AS

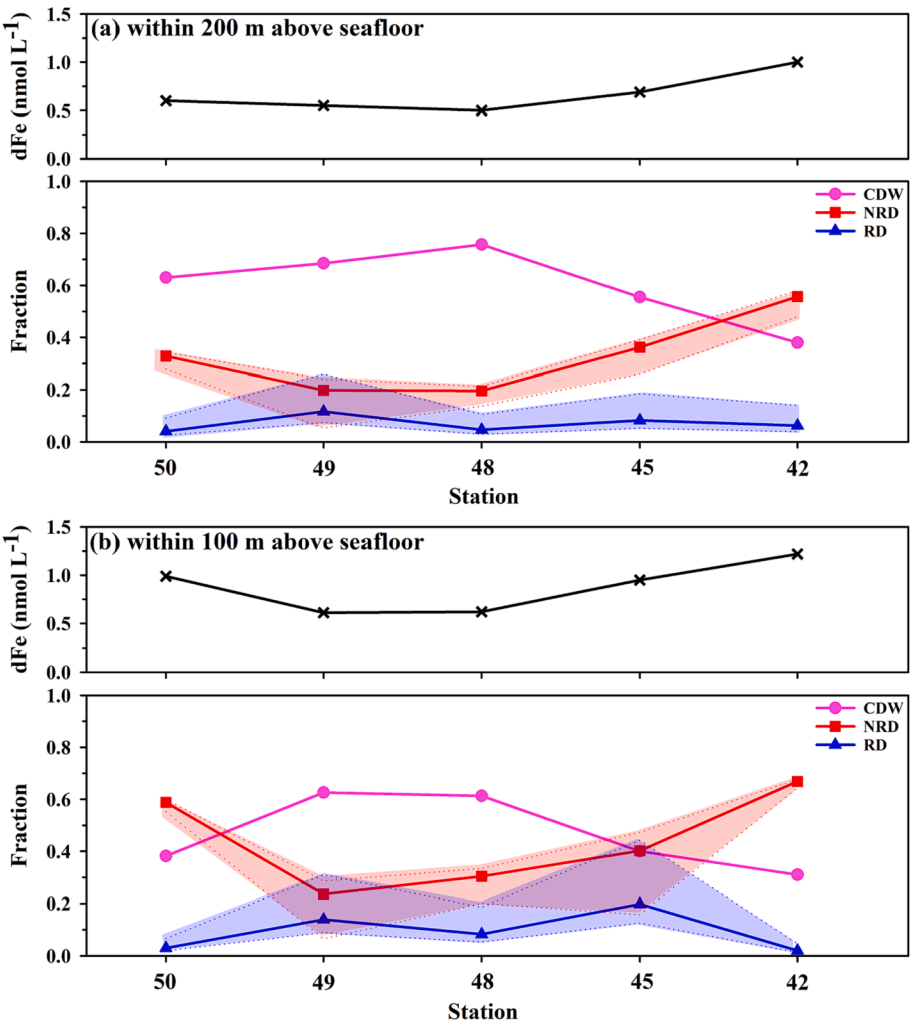

Fig. 5. Fractions of reductive dissolution (RD) (f'_{RD}), non-reductive dissolution (NRD) (f'_{NRD}) and circumpolar deep water (CDW) (f_{CDW}) and [dFe] at the GPpr12 DIS (inflow) stations (in each depth interval the means were calculated). RD (blue triangle), NRD (red square), and CDW (pink dot) corresponds to left y-axis; whereas dFe (black solid line) corresponds to the right y-axis. For RD, three different endmembers are used to account for the uncertainties – solid line (–2.2 ‰) and upper and lower estimates (–0.93 ‰ and –3.5 ‰). The coloured shading indicates the range, simply based on interpolation of the upper and lower estimates. (a) samples located within 200 m above the seafloor; (b) samples located within 100 m above the seafloor.

have been experiencing rapid collapsing and melting (Gourmelen et al., 2017; Jacobs et al., 1996; Jenkins et al., 2010; Rignot et al., 2008). It was previously proposed that rapid melting of glaciers and ice sheets could be an important source of Fe (Alderkamp et al., 2012; Gerringa et al., 2020a, 2020b, 2012). For example, Sherrell et al. (2015) observed elevated dFe (0.62–0.77 nmol L^{-1}, 80–600 m) in the mCDW outflow from the DIS compared to surface polynya waters (~0.15 nmol L^{-1}), likely sourced from a combination of mCDW, shelf sediments, and DIS-sourced dFe. This [dFe] range is comparable to [dFe] observed in the mCDW outflow in this study (0.64 ± 0.06 nmol L^{-1}, 195–294 m, Stn 36). However, from our previous work, the addition of DIS-sourced dFe itself to the mCDW outflow was estimated to be negligible (van Manen et al., 2022). In fact, [dFe] effectively decreased slightly in the outflow compared to the inflow (average of 0.99 ± 0.17 (n = 3) vs 0.64 ± 0.06 (n = 3) nmol L^{-1}; Fig. 4), likely due to extensive mixing of the dFe-rich outflow with relatively low dFe water close to the ice shelf, based on a conservative mixing model (van Manen et al., 2022). However, the observations from van Manen et al. (2022) were solely based on [dFe] and as such, any change in [dFe] underneath the DIS due to biogeochemical processes or from different sources/sinks remained unconstrained. Therefore, although the δ^{56}Fe of cryospheric sources and processes involved remain relatively poorly constrained (Fitzsimmons and Conway, 2023), in the following section we attempt to use δ^{56}Fe to investigate the sources of dFe and potential biogeochemical processes in the ice shelf cavity.

4.2.1. *Is conservative mixing (or addition of heavy Fe) driving dissolved δ^{56}Fe underneath the DIS?*

In our study, we observed a change in δ^{56}Fe of –0.70 ± 0.13 to –0.23 ± 0.15 ‰ between DIS inflow and outflow ($\Delta\delta^{56}Fe_{DIS}$ of +0.47 ‰), coupled with the decline in [dFe] of ~1 to 0.6 nmol kg^{-1} that was previously attributed to the effects of conservative mixing (van Manen et al., 2022). To evaluate whether conservative mixing can feasibly explain this observed change in the δ^{56}Fe distribution underneath/adjacent to the DIS (or whether other processes are required), we compared δ^{56}Fe values from four water masses (defined as endmembers from representative samples) that are most probably the main components involved in conservative mixing:

(1) mCDW inflow: we chose a Θ isotherm of 0 °C which is ~ 100 m above the seafloor (usually around 500 m) for the $DIS_{(inflow)}$ stations to represent the mCDW inflow (Fig. 3a). This depth interval for the mCDW inflow has been previously described for this region (Miles et al., 2016; Sherrell et al., 2015; van Manen et al.,

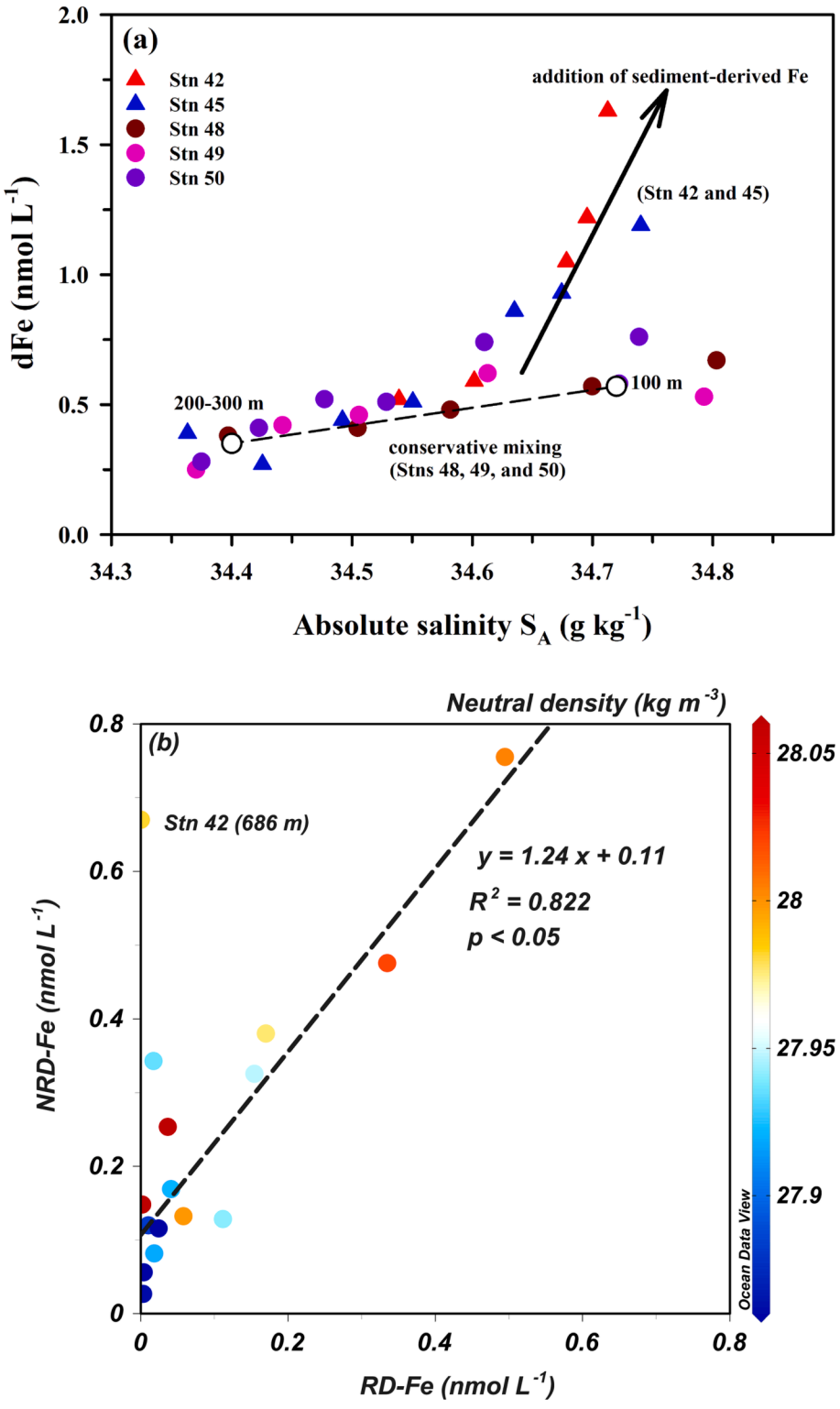

Fig. 6. Relationship of [dFe] and absolute salinity (SA), dFe derived from non-reductive dissolution (NRD-dFe) and from reductive dissolution (RD-dFe) (coloured for neutral density) within 300 m above the seafloor, of the GPpr12 DIS(inflow) stations. (a) [dFe] versus S_A. Solid coloured dots and triangles represent stations relatively far from the DIS (Stn 48, 49, and 50) and stations close to the DIS (Stn 42 and 45), respectively. Empty black dots represent the averages (within 100 m above the seafloor and 200–300 m above the seafloor) from Stn 48, 49, and 50; whereas the black arrow and the dashed line indicate the addition of sediment-derived Fe and the conservative mixing line, respectively. (b) NRD-dFe versus RD-dFe. The dashed line represent the regression line. Note that the correlation excludes Stn 42 (689 m).

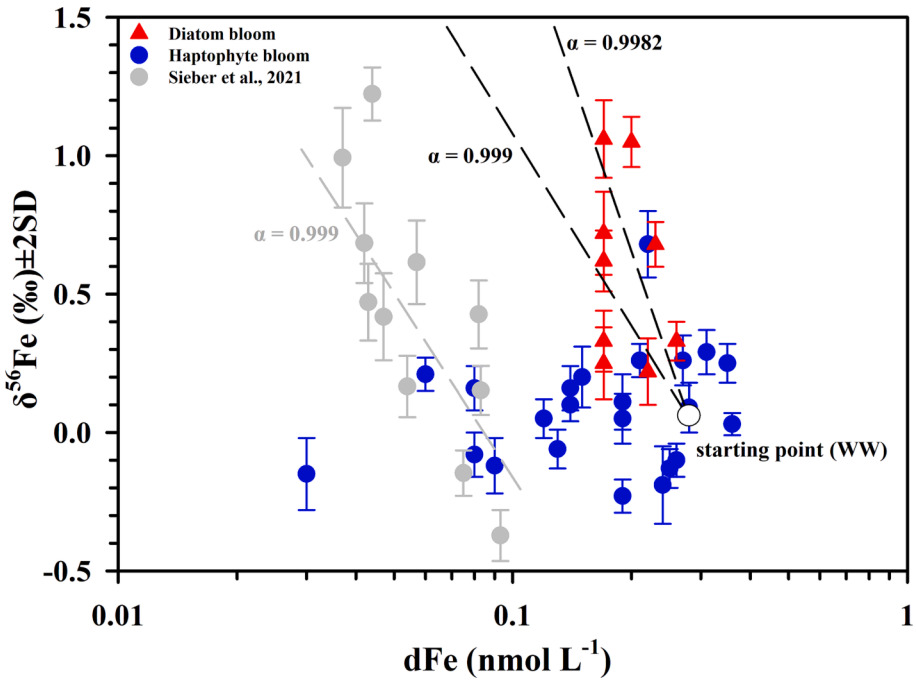

Fig. 7. Fe isotope systematics in the surface layer of the GPpr12 'bloom' stations (red: GIS diatom bloom; blue: DIS haptophyte bloom), in comparison with data derived from Mertz glacier polynya (Sieber et al., 2021). The dashed lines represent predicted Rayleigh fractionation trends with different fractionation factors ($\alpha = R_{biomass}/R_{seawater}$) based on a defined starting point (empty white dot, observed [dFe] and δ^{56}Fe values in winter water).

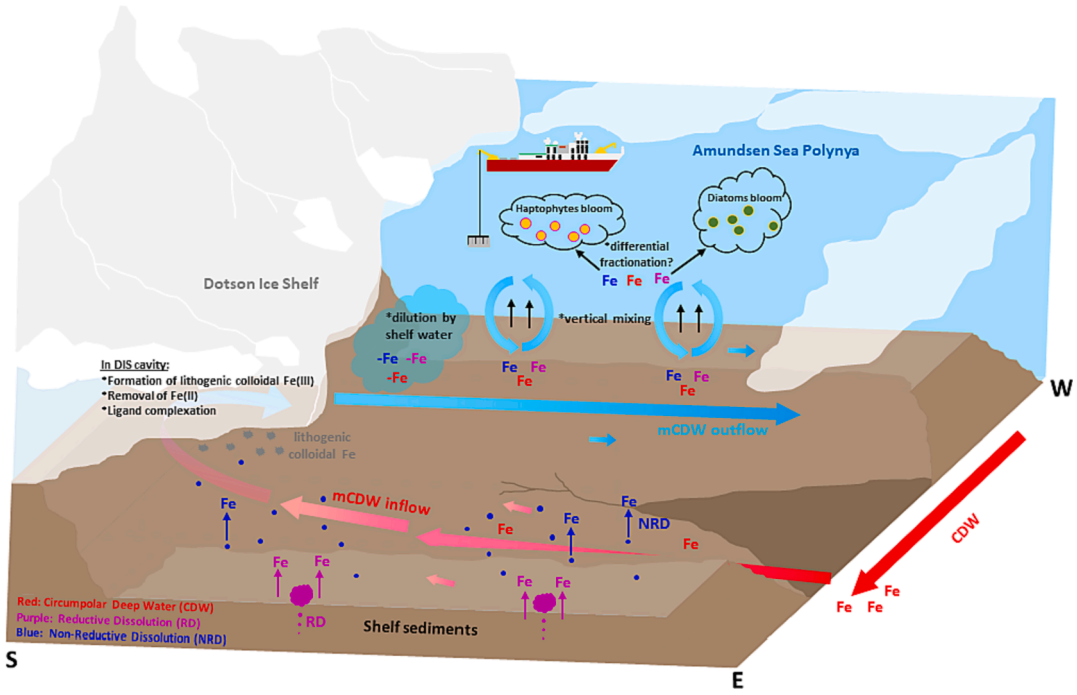

Fig. 8. Conceptual summary of the sources and biogeochemical processes of dFe in the ASP.

2022), and is characterized by $\delta^{18}O$ (>–0.2 ‰) and high S_A (>34.5) (Fig. 3a and b). This depth interval is also comparable to the depth of the grounding line of the DIS (~420–500 m, Jordan et al., 2020). To represent the properties of the mCDW inflow prior to entering the ice cavity, we selected samples at Stn 45 (442–507 m). The Fe isotopic composition of the defined mCDW inflow endmember ($\delta^{56}Fe_{inflow}$) is –0.70 ± 0.13 ‰ (mean ± 1 SD) (Table 2). Here, it should be noted that we choose Stn 45 over Stn 42 (i.e., the closest station to the DIS in the mCDW inflow) to represent the mCDW inflow better because the samples in deep water at Stn 42 were found to be affected by lithogenic material from the DIS and perhaps also by mCDW outflow (based on elevated dissolved Fe and particulate Fe concentrations; van Manen et al., 2022); this assertion is also supported by a δ^{56}Fe anomaly (close to 0 ‰) observed between 690 and 715 m at Stn

Table 2
Endmembers selected for Section 4.2.1. Between these three $\delta^{56}Fe$ endmembers based on averaged observations ($\delta^{56}Fe_{outflow}$, $\delta^{56}Fe_{inflow}$, and $\delta^{56}Fe_{shelfwater}$), there was a significant difference ($p < 0.05$), determined using a test of analysis of variance (one-way ANOVA), where a follow-up Post-Hoc test (Bonferroni correction) showed that $\delta^{56}Fe_{inflow}$ differed significantly from (was lighter than) the other two endmembers ($\delta^{56}Fe_{outflow}$ and $\delta^{56}Fe_{shelfwater}$).

Endmember	Station	Depth (m)	$\delta^{56}Fe \pm 2$ SD (‰)	Θ (°C)	S_A (g kg^{-1})
$\delta^{56}Fe_{inflow}$	45	442	–0.64 ± 0.05	–0.02	34.64
		467	–0.61 ± 0.06	0.14	34.67
		507	–0.85 ± 0.04	0.43	34.74
		Mean ± 1 SD	–0.70 ± 0.13	0.18 ± 0.23	34.68 ± 0.05
$\delta^{56}Fe_{shelfwater}$	42	145	–0.19 ± 0.14	–1.42	34.16
		245	–0.15 ± 0.05	–1.52	34.24
		344	–0.32 ± 0.09	–1.44	34.33
		Mean ± 1 SD	–0.22 ± 0.09	–1.46 ± 0.05	34.24 ± 0.09
$\delta^{56}Fe_{outflow}$	36	195	–0.07 ± 0.06	–1.04	34.24
		245	–0.27 ± 0.06	–0.72	34.32
		294	–0.36 ± 0.07	–0.54	34.389
		Mean ± 1 SD	–0.23 ± 0.15	–0.77 ± 0.25	34.32 ± 0.07

42, different from the samples above and below (Fig. 4), indicating a lithogenic signal at this depth.

(2) ice shelf meltwater: the meltwater from the ice shelf where the melting is induced by inflow of relatively warm mCDW. Since we do not have direct measurements of meltwater, this water mass has an unknown Fe isotopic composition ($\delta^{56}Fe_{icemelt}$) that will be further evaluated in this section.

(3) shelf water: we defined a water mass geographically adjacent to the ice shelf, which mixes with the mCDW inflow and ice shelf meltwater as a third component for the conservative mixing model. The Fe isotopic composition of the shelf water endmember ($\delta^{56}Fe_{shelfwater}$) is –0.22 ± 0.09 ‰ (mean ± 1 SD) (Table 2). Samples collected at similar depth as the mCDW outflow, but outside the region where outflow occurs, were chosen to represent the endmember for shelf water (Stn 42, 145–300 m, Figs. 2 and 3a). The rationale of choosing Stn 42 is that it is the station closest to the DIS that thus may best exhibit the properties of this water immediately prior to mixing. This shelf water has similar Θ and S_A to WW (Fig. 2).

(4) mCDW outflow: the water mass that is the result of conservative mixing between the mCDW inflow, shelf water, and ice shelf meltwater. This outflowing water mass was identified below ~200 m at Stn 36, based on elevated Θ (>–1°C), $\delta^{18}O$ (~–0.4 ‰), and S_A (>34.1), compared to the remainder of the water column (Figs. 2, 3a and b). The Fe isotopic composition of the defined mCDW outflow endmember ($\delta^{56}Fe_{outflow}$) is –0.23 ± 0.15 ‰ (mean ± 1 SD) (Table 2). Since samples below 400 m at Stn 36 were not available due to a technical issue with the sampling system, we chose samples collected between 200 and 400 m at this station to represent the mCDW outflow. This depth interval is comparable to previously reported depths for the core of mCDW outflow in the same region (Miles et al., 2016; Randall-Goodwin. et al., 2015).

Previously, the fractions of each water mass were estimated based on $\delta^{18}O$, where the mCDW inflow, ice shelf meltwater, and shelf water, accounted for 74.9 %, 0.6 %, and 24.5 %, respectively (Tian et al., 2023). Based on these estimated fractions and selected endmembers, $\delta^{56}Fe_{icemelt}$ can be estimated (assuming conservative mixing) based on the following mixing model:

$$0.749 \times \delta^{56}Fe_{inflow} + 0.245 \times \delta^{56}Fe_{shelfwater} + 0.006 \times \delta^{56}Fe_{icemelt} = \delta^{56}Fe_{outflow} \quad (5)$$

Using this equation, we calculated a $\delta^{56}Fe_{icemelt}$ endmember of +5.78 ‰. Although there is a paucity of data for $\delta^{56}Fe$ values in Antarctic glacial systems (Henkel et al., 2018; Mikucki et al., 2004; Sieber et al., 2021), and the variability in dissolved $\delta^{56}Fe$ in meltwater is highly dependent on subglacial weathering (physical and chemical) in individual glacial systems (Krisch et al., 2021; Stevenson et al., 2017; Zhang et al., 2015), a value of +5.78 ‰ is clearly unfeasible for $\delta^{56}Fe_{icemelt}$, which is more likely close to crustal $\delta^{56}Fe$ (+0.09 ‰; Beard and Johnson, 2004) as most Fe in an ice shelf derives from lithogenic materials when the ice sheets move towards the shore and interact with the underlying bedrock (Raiswell et al., 2006), or perhaps slightly isotopically lighter due to reductive dissolution. Indeed, van Manen et al. (2022) found the mCDW outflow was enriched in refractory particulate Fe (most likely lithogenic Fe) compared to labile particulate Fe and dissolved Fe. Further, +5.78 ‰ is much heavier than any $\delta^{56}Fe$ values reported for any dFe source in the marine system (Fitzsimmons and Conway, 2023; Johnson et al., 2020). If we instead assign a crustal signature to $\delta^{56}Fe_{icemelt}$ (+0.09 ‰), the constrained contribution of 0.6 % from ice shelf melt could not result in the $\delta^{56}Fe_{outflow}$ as observed – the estimated overall $\delta^{56}Fe$ signal in the outflow would be –0.61 ‰, which is much lighter than the observed $\delta^{56}Fe_{outflow}$ (–0.23 ± 0.15 ‰). Obviously, choosing a lighter endmember for $\delta^{56}Fe_{icemelt}$ would only exacerbate this issue. Thus, although conservative physical mixing with shelf water provides a plausible explanation for the observed [dFe] changes between the inflow and outflow, it cannot explain the observed positive change in $\delta^{56}Fe$ (at best only a $\Delta\delta^{56}Fe$ of +0.09 ‰, from –0.70 to –0.61 ‰). Instead, other processes must be driving an apparent fractionation in dissolved $\delta^{56}Fe$ within the DIS system.

Indeed, it has been hypothesized, based on Arctic systems, that the residence time of inflowing water underneath ice shelf/glacier system may enable significant chemical alternation (e.g., changes in nutrient availability and/or input of ice sheet-derived materials) between the inflow and the outflow, especially for non-conservative elements (e.g., Fe) (Krisch et al., 2021), especially if the residence time of water is long. For example, the residence time of inflowing water masses underneath the '79°N Glacier' is around 5.4 months (Schaffer et al., 2020). Krisch et al. (2021) suggested that thermodynamic equilibrium between dFe, labile particulate Fe, and ligands in the ice cavities could play an important role in subglacial nutrient supply as well as driving the $\delta^{56}Fe$ of the dFe pool to heavier values than known Fe sources. Although the residence time of the mCDW inflow underneath the DIS is much shorter than the '79°N Glacier' (estimated to only be approximate 2 months; Girton et al., 2019; Yang et al., 2022), our isotopic data imply that, in addition to ice shelf-derived Fe and mixing with shelf water, processes occurring underneath the DIS may be responsible for an additional $\delta^{56}Fe$ shift ($\Delta\delta^{56}Fe$ of at least +0.38 ‰, from –0.61 to –0.23 ‰), which cannot be easily explained by simple addition of dFe without further

fractionation.

4.2.2. Potential processes occurring underneath the DIS leading to heavier Fe in the outflow

While understanding the fractionation of Fe isotope ratios resulting from different processes in the oceans is the subject of ongoing investigations (Fitzsimmons and Conway, 2023), studies have identified various internal cycling processes that could result in isotopic fractionation of the dissolved pool. Here, we evaluate several processes that could potentially result in a shift towards isotopically heavy dFe ($\Delta\delta^{56}Fe = +0.38$ ‰) underneath the DIS; these include the enhanced preservation and addition of lithogenic colloidal Fe(III) together with the preferential loss of Fe^{2+}, and complexation with Fe-binding ligands.

Preferential preservation of one Fe species over another underneath the ice shelf could result in an overall change in the $\delta^{56}Fe$ of the whole dFe pool. For example, addition and preservation of 'lithogenic' derived colloidal Fe(III) that is matched by an equivalent loss of Fe^{2+} or Fe(III) species could be responsible for an overall change in 'dissolved' $\delta^{56}Fe$. Previously, the speciation of NRD-dFe as lithogenic colloidal Fe(III) has been highlighted by Homoky et al. (2021) who observed near-crustal $\delta^{56}Fe$ in the colloidal fraction in core-top porewater and suggested such colloidal Fe is likely formed by weathering of lithogenic particles via a non-reductive process. In this study, benthic sediments supply both particles and NRD-derived dFe (see Section 4.1.1), and ice shelf melt (or glacial melt) supplies a significant amount of particulate Fe into the AS via the mCDW outflow (Gerringa et al., 2012, 2020b; Planquette et al., 2013; van Manen et al., 2022). Notably, particulate Fe concentrations ([pFe]) were two to three orders of magnitude higher than [dFe] in the AS, and elevated [pFe] was observed especially in the $DIS_{(outflow)}$ stations (van Manen et al., 2022), with refractory [pFe] (34.4 ± 11.4 nmol/L, 2 SD) and labile [pFe] (12.6 ± 2.2 nmol/L, 2 SD) relative to 0.6 nM [dFe]. Such high loading of pFe could facilitate exchange of Fe between the dissolved pool and labile particulate pool ('a reversible equilibrium'; Fitzsimmons et al., 2017; van Manen et al., 2022), acting to 'reset' or moderate dissolved $\delta^{56}Fe$ signatures whilst [dFe] stays relatively stable. This idea is consistent with previous suggestions that isotopic composition can be modified due to extensive exchange between particles and seawater whilst dissolved concentrations do not change significantly; this concept, termed 'boundary exchange', was observed for Neodymium isotope systematics (e.g., Lacan and Jeandel, 2005) and later inferred for other trace metals (e.g., Fe, Jeandel, 2016), as well as being observed in deep nepheloid layers of the North Atlantic, where dissolved $\delta^{56}Fe$ values approach crustal composition with no accompanying change in [dFe] (Conway and John, 2014). It has also been observed that isotopically light Fe^{2+} (ranging from –0.89 to –0.12 ‰) released from basal meltwater and/or subglacial discharge was lost during extensive reworking of Fe phases (e.g., dissolved, ligand-bound, particulate and sedimentary phases) in the glacial cavity of the '79°N Glacier', leading to a near-crustal $\delta^{56}Fe$ signature (+0.07 ± 0.09 ‰) in the glacial outflow (Krisch et al., 2021) where sediment resuspension in nepheloid layers of the ice cavity was suggested a main driver of lithogenic Fe input (Chen et al., 2022). This observation implies that the loss of Fe^{2+} may be more significant than the addition of Fe(III) species underneath the ice sheet systems, especially in systems where particle loading is prominent (van Manen et al., 2022).

Organic ligand complexation could also contribute to the change in $\delta^{56}Fe$ under the ice shelf. Complexation of Fe by organic ligands tends to bind isotopically heavy Fe, leading to high $\delta^{56}Fe$ values for the dissolved Fe pool, especially due to ligands with a strong affinity for Fe (e.g., siderophores) (Dideriksen et al., 2008; Morgan et al., 2010). Additionally, although the jury remains out on the effect of particle scavenging on $\delta^{56}Fe$, with limited open ocean studies showing negligible to only small fractionation (0 to –0.3 ‰ Fitzsimmons and Conway, 2023; Radic et al., 2011), particle dissolution coupled to organic-ligand complexation as well as scavenging has been invoked to explain isotopically heavy dFe in North Atlantic surface waters (+0.8 ‰, Conway and John, 2014; John and Adkins, 2012). In the AS, Thuróczy et al. (2012) found organic ligands (originating from mCDW and/or sediments) to be nearly saturated with Fe near the ice shelves of Pine Island Glacier, with only modest capacity for complexing additional dFe from glacial meltwater. Under such conditions, the ligands are already saturated before the mCDW enters the ice shelf cavity, leaving little capacity for either complexation or a role in adjusting the composition of dissolved $\delta^{56}Fe$. However, in the DIS outflow, van Manen et al. (2022) showed that ligand to dFe ratios were above two at Stns 36 and 42, indicating Fe-binding ligands were unsaturated, which implies a potential for ligands to bind additional dFe under the ice shelf. However, that study also showed that even though the outflow was rich in Fe-binding ligands, dFe did not seem to increase in contrast to particulate Fe, implying the ligands were not strong enough to compete with adsorption onto particles that were also supplied from ice shelf melt (van Manen et al., 2022), consistent with a possible preferential loss of reactive species such as Fe^{2+} or Fe(III) species, balanced by an increase in lithogenic colloids under the DIS. A similar scenario of weak complexation by organic ligands compared to particle scavenging was also observed near the terminus of the '79°N Glacier' (Ardiningsih et al., 2020). However, even if ligands are not strong enough to effectively compete with particle scavenging in the ASP, and weak ligands would be expected to drive a smaller fractionation factor than strong ligands (Morgan et al., 2010), they could still play a role in setting the resulting overall isotopic signature of the dFe pool in the DIS outflow.

Overall, although we cannot tease out the effects of these competing processes, we propose that particles, together with colloids from NRD-dFe, contribute 'lithogenic' colloidal Fe(III) (with near-crustal $\delta^{56}Fe$) to the dissolved pool in the DIS outflow, with particles also likely scavenging truly dissolved Fe species (e.g., Fe^{2+}) in competition with Fe binding ligands. The net effect of these processes on the isotopic composition would be to drive dissolved $\delta^{56}Fe$ towards crustal values under the DIS, as was observed at the '79°N Glacier' (Krisch et al., 2021).

4.3. Fractionation of Fe isotopes in ASP phytoplankton blooms

Phytoplankton blooms are an annual feature in the ASP during austral spring and summer (Alderkamp et al., 2015; Arrigo et al., 2012; Park et al., 2017) where the surface dFe distribution was found to be the opposite of the distribution of phytoplankton mass (Alderkamp et al., 2012). In our study in the surface layer of both the DIS and GIS regions, low [dFe] also coincided with elevated fluorescence, indicative of phytoplankton blooms (Figs. 3 and 4). It is thus likely biological uptake is the main process driving the drawdown of dFe in the surface ASP (Alderkamp et al., 2012; Sherrell et al., 2015; van Manen et al., 2022). Biological uptake may also affect dissolved Fe isotopic composition. We observed elevated remnant dissolved $\delta^{56}Fe$ in the surface layer of the GIS bloom (up to +1.06 ‰), that was significantly higher than that following the DIS bloom (~+0.68 ‰) ($p < 0.05$, Table 2). Generally, isotopically heavier remnant dFe following biological uptake is consistent with the limited previous studies that looked at blooms or the effect of uptake (Ellwood et al., 2020; Ellwood et al., 2015; Sieber et al., 2021).

The difference in $\delta^{56}Fe$ between blooms could result from the extent of Fe uptake in the surface layer, namely, with more dFe assimilated, one might expect to observe heavier $\delta^{56}Fe$ in seawater – Yager et al. (2016) argued that a longer opening time of the polynya may lead to higher Fe uptake, hence potentially also a stronger biological-driven isotope fractionation effect. Here, we compared [dFe] in the pre-bloom stage (estimated starting concentrations) and the bloom stage (observed concentrations) to evaluate the Fe uptake in the DIS and GIS bloom respectively. The sampling period for the two blooms was from 24th January to 2nd February. For the pre-bloom stage, we assume [dFe] in WW ($\Theta < -1.5$ °C) represented the starting concentrations as WW is a remnant of the cold winter mixed layer overlain by a relatively warm and fresh AASW that forms from WW by sea ice melting and warming due to incident irradiance during summer (e.g., Mosby, 1936). The

Table 3
Comparison of δ^{56}Fe, [dFe], and POC and PON, in the surface layer of two ASP blooms. Starting [dFe] is estimated based on [dFe] in WW ($\Theta < -1.5$ °C). Note that WW samples for determining the starting [dFe] were selected from the $GIS_{(inflow)}$ stations and the $DIS_{(inflow)}$ stations (except Stn 42 due to extensive particles exported from the DIS that could already alter [dFe] (e.g. scavenging and regeneration, van Manen et al., 2022). All values are presented as mean ± 1 SD.

The surface layer	DIS bloom	GIS bloom	t-Test (two-tail)
Observed δ^{56}Fe (‰)	+0.08 ± 0.20 (n = 27)	+0.58 ± 0.33 (n = 9)	P < 0.05
Starting [dFe] (nmol L^{-1})	0.30 ± 0.05 (n = 12)	0.26 ± 0.05 (n = 12)	P = 0.07
Observed [dFe] (nmol L^{-1})	0.20 ± 0.09 (n = 28)	0.18 ± 0.05 (n = 10)	P = 0.60
POC (integrated) (g m^{-3})	3.87 ± 1.82 (n = 3)	1.80 ± 0.21 (n = 3)	P = 0.32
PON (integrated) (g m^{-3})	25.3 ± 12.1 (n = 3)	8.86 ± 1.03 (n = 3)	P = 0.29

comparison is detailed in Table 3. The results showed no statistically significant difference of starting [dFe], nor of observed [dFe], between the DIS and GIS bloom (Table 3), suggesting a comparable amount of Fe uptake between two blooms (assuming there were no differences in supply during the bloom period). Additionally, integrated particulate organic carbon (POC) and nitrogen (PON) concentrations are also not significantly different between two regions (Table 3), implying that primary production was likely at comparable levels in the two blooms. Therefore, a differential degree of Fe uptake with the same fractionation factor cannot explain the observed difference in δ^{56}Fe in the surface layers of the two regions (Table 3).

Alternatively, different phytoplankton communities in the two blooms could potentially fractionate Fe isotope ratios via different fractionation factors during uptake (Ellwood et al., 2015). Pigment-based phytoplankton taxonomic composition analysis showed that the dominant phytoplankton species differed between the blooms; haptophytes dominated the DIS bloom (64–94 % of total abundance), whereas diatoms dominated the GIS bloom (40–91 % of total abundance) (Supplementary Fig. S2). We thus hypothesize that the difference in remnant surface dissolved δ^{56}Fe between blooms could result from different dominant phytoplankton communities. Although there is little understanding about how different species fractionate Fe via biological uptake, the utilization of Fe and uptake mechanisms by phytoplankton are better constrained. For example, diatoms and haptophyte species have different strategies in terms of utilizing Fe and may allocate resources (e.g., Fe and other nutrients) distinctly (Alexander et al., 2015; Litchman et al., 2007; Margalef, 1978). For instance, diatoms tend to maximize growth rates under nutrient-replete environments (Endo et al., 2018), whereas haptophytes allocate nutrients not only to reproduction but also to other activities to maintain a constant population size (Endo et al., 2018; Parry, 1981). Such diversity in the use of Fe between diatoms and haptophytes implies they assimilate Fe via different pathways, such as transporters for specific Fe compounds, direct Fe(II) transporters, or reduction of Fe(III) to Fe(II) on the cell surface (e.g., ligand-bound Fe) (Hutchins et al., 1999; Morel et al., 2008), which could result in different isotopic fractionation factors. Moreover, Ellwood et al. (2015) pointed out that small phytoplankton (e.g., Synechococcus) and large phytoplankton (e.g., diatoms) may cause isotopic fractionation at different levels. Similarly, the size of haptophytes (generally < 5 μm) and diatoms (2–200 μm) is markedly different (e.g., Cuvelier et al., 2010; Halse and Syvertsen, 1996; Masquelier et al., 2011), implying haptophytes and diatoms might induce different Fe isotopic effects during assimilation. However, further investigations such as culture experiments on biological fractionation by these two common Southern Ocean phytoplankton are required to support our speculation.

Although biological uptake is considered to be the main process controlling [dFe] in the surface of the ASP (Alderkamp et al., 2015; van Manen et al., 2022; this study), we do not exclude the idea that other processes may also influence surface dissolved δ^{56}Fe. If biological uptake was the dominant process fractionating dFe isotopes in the bloom under a closed system, the isotopic fractionation could be described with a Rayleigh fractionation factor. Previously, such a trend was observed and the fractionation factor (α) ($\alpha = R_{biomass}/R_{seawater}$) of biological uptake was predicted to range from 0.9977 to 0.9990 in Southern Ocean eddies (Ellwood et al., 2020) and in the Mertz Glacier Polynya (α = 0.999, Sieber et al., 2021). In our δ^{56}Fe data, while the dFe systematics of the GIS diatom bloom can be described using a closed Rayleigh model with an α of between 0.9982 and 0.9990 (except Stn 24), the DIS haptophyte bloom cannot be described simply in this way (Fig. 7). This suggests that biological assimilation may be a dominant factor in the fractionation of dFe in the GIS bloom, but not in the DIS bloom. This disparity could imply that any biological fractionation in the DIS region is overprinted by other dFe sources (e.g., icebergs and ice shelves), rendering the assumption of a closed system less valid, or that uptake by haptophytes does not follow a simple Rayleigh trend. When comparing the two regions, both meteoric water input and higher refractory particulate Fe input were estimated to be higher in the DIS region (van Manen et al., 2022), potentially suppling more dFe with a lithogenic isotopic signature (~0 ‰) to the DIS bloom and buffering the isotopic composition of the remnant dFe pool (Fig. 4). Alternatively, other processes such as rapid recycling (e.g., adsorption and regeneration), bacterial regeneration, and complexation with organic ligands may also play a role in fractionating Fe along with biological uptake (Ellwood et al., 2015; Sieber et al., 2021), resulting in a non-Rayleigh fractionation trend in the DIS bloom. Indeed, a combination of these factors was found to best explain surface data previously in Southern Ocean eddies by Ellwood et al. (2020). Overall, while our findings do provide support for uptake of light Fe and also for variable fractionation factors between species, our results suggest that the role of biogeochemical conditions (the interplay of biological uptake and other processes) in setting surface δ^{56}Fe are variable in the surface ASP and likely between Antarctic polynyas.

5. Conclusions

In this study, we characterized Fe isotope systematics in one of the most productive Antarctic coastal polynyas (the ASP), focusing on external Fe sources, the change of [dFe] and δ^{56}Fe in the Dotson ice shelf system that experiences rapid melting due to the intrusion of mCDW, and Fe isotopic fractionation resulting from different phytoplankton blooms (summarized in Fig. 8). By utilizing the isotopic composition of Fe, we show that two sedimentary processes (RD and NRD) both supply dFe from benthic sediments into overlying mCDW within the AS. Additionally, we show that while NRD is a more important process than RD for releasing dFe from benthic sediments into overlying waters in the AS (with 20–56 % from NRD and 4–12 % from RD), both are derived from sediment resuspension. While inflowing mCDW is enriched in dFe from sediments, the DIS itself does not appear to add any extra dFe, previously attributed to the mixing of the outflow with relatively Fe-poor shelf waters. From an Fe isotopic perspective, however, a concomitant observed change in δ^{56}Fe cannot be explained solely by conservative mixing with low [dFe] shelf water. Instead, we propose that [dFe] and δ^{56}Fe are affected by a combination of enhanced preservation and addition of lithogenic colloidal Fe(III) together with the differential loss of Fe^{2+} and complexation with Fe-binding ligands, driving δ^{56}Fe to heavier values in the outflow than the inflow. The phytoplankton bloom regions in the ASP displayed distinct Fe isotopic signatures in the surface layer where δ^{56}Fe is much heavier in the diatom

(GIS) bloom compared to the haptophyte (DIS) bloom. Based on our field data, we speculate that haptophytes and diatoms may fractionate Fe differently or to different extent due to different uptake mechanisms for Fe, however, this requires further investigation, for example using culture experiments. Furthermore, we found that, even in productive surface waters, differences in dissolved δ^{56}Fe are not likely to be controlled by biological activity alone; external sources (e.g., particulate and dissolved Fe input from ice shelf melt) and various other biogeochemical processes such as adsorption and regeneration, and complexation with organic ligands also likely play a role.

Overall, our isotopic data provides insights about the external sources of Fe, the role of the DIS in regional Fe cycling, and potential biological fractionation effects within phytoplankton blooms. However, it is worth noting that the ASP is a complex and understudied system in terms of nutrient cycling, biological activity and mixing of different water masses. Therefore, any prediction about how ongoing rapid changes in Antarctic coastal regions (e.g., nutrient supply) will affect marine ecosystems (notably phytoplankton communities) remains challenging and speculative. For example, as ice shelf melting increases due to increased inflow of mCDW (Jacobs et al., 2011; Mankoff et al., 2012), more ice shelf-derived particles are expected in the water column, but in how far this affects the current dissolved-particulate balance is unknown. Hence, we do not have enough information to predict how Fe sources and sinks might change, nor what the net effect would be on dFe cycling in this region. Additionally, increasing CDW intrusion would also result in increasing supply of other bio-active metals, such as Zn, Cd, and Co since CDW is a major source of various metals to the ASP (Sherrell et al., 2015; Tian et al., 2023; van Manen et al., 2022). As a result, the dominant species of phytoplankton blooms could experience several shifts in species composition over a longer bloom period as susceptibility to (co-)limitation (e.g., Fe and B_{12}, and the requirements for various metals differs between different species, Bertrand et al., 2007; Bertrand et al., 2015). However, we have little knowledge on how these shifts would affect the cycling of various bio-active metals or how the availability of bio-active metals influences community composition and the development of phytoplankton blooms in the ASP. Thus, while continued climate change will undoubtedly affect the biogeochemical cycling of trace metals in the ASP, sustained interdisciplinary investigations are required to better understand this system and predict the local and global consequences of changes in the ASP.

6. Data availability

Research data has been supplied via a repository: https://doi.org/10.25850/nioz/7b.b.bd.

Declaration of Competing Interest

The authors declare that they have no known competing financial interests or personal relationships that could have appeared to influence the work reported in this paper.

Acknowledgments

This work was supported by the Dutch Research Council (NWO) (grant number: ALWPP.2016.020 to RM), the U.S. National Science Foundation (Award OCE2123354 to TMC), and Scientific Committee on Oceanic Research (SCOR, grant number: OCE-1840868). We thank the captain and the crew of the R/V Araon, as well as all the scientists on board, for their assistance and support during the expedition ANA08B (project number: PE21110) with the R/V Araon provided by the Korea Polar Research Institute (KOPRI). We also thank Matthias Sieber and Ethan Goddard from the College of Marine Science, University of South Florida, the USA, for the assistance with MC-ICP-MS analysis, as well as Sven Ober and colleagues from NIOZ National Marine Facilities (NMF) for the preparation of Titan CTD and other facilities used during this expedition. Piet ter Schure and his team from DMT Marine Equipment are acknowledged for their great help with the winch setup for the Titan sampling system used on R/V Araon.

Appendix A. Supplementary material

This supplementary material includes Table S1 – Results of the estimation of individual fractions of reductive dissolution (RD), non-reductive dissolution (NRD), and Circumpolar Deep Water (CDW) within 200 m above the seafloor and within 100 m above the seafloor. Fig. S1 – Linear regressions of dissolved Fe concentrations ([dFe]) derived from ICPMS (Element 2) versus concentrations derived from ICPMS (Neptune Plus) for ANA08B expedition, and Fig. S2 – Abundance of different phytoplankton groups in the surface layer of all GPpr12 stations included in this study including the $DIS_{(inflow)}$ stations (Stn 49, 45, and 42), the $DIS_{(outflow)}$ stations (Stn 36, 34, and 33), and the $GIS_{(inflow)}$ stations (Stn 55, 24, and 57). Supplementary material to this article can be found online at https://doi.org/10.1016/j.gca.2023.10.029.

References

Abadie, C., Lacan, F., Radic, A., Pradoux, C., Poitrasson, F., 2017. Iron isotopes reveal distinct dissolved iron sources and pathways in the intermediate versus deep Southern Ocean. Proc. Natl. Acad. Sci. 114, 858–863.

Alderkamp, A.-C., Mills, M.M., van Dijken, G.L., Laan, P., Thuróczy, C.-E., Gerringa, L.J. A., de Baar, H.J.W., Payne, C.D., Visser, R.J.W., Buma, A.G.J., Arrigo, K.R., 2012. Iron from melting glaciers fuels phytoplankton blooms in the Amundsen Sea (Southern Ocean): Phytoplankton characteristics and productivity. Deep Sea Res. Part II 71–76, 32–48.

Alderkamp, A.-C., van Dijken, G.L., Lowry, K.E., Connelly, T.L., Lagerström, M., Sherrell, R.M., Haskins, C., Rogalsky, E., Schofield, O., Stammerjohn, S.E., Yager, P. L., Arrigo, K.R., 2015. Fe availability drives phytoplankton photosynthesis rates during spring bloom in the Amundsen Sea Polynya, Antarctica. Elementa: Sci. Anthropocene 3, 000043.

Alexander, H., Rouco, M., Haley, S.T., Wilson, S.T., Karl, D.M., Dyhrman, S.T., 2015. Functional group-specific traits drive phytoplankton dynamics in the oligotrophic ocean. Proc. Natl. Acad. Sci. 112, E5972–E5979.

Ardiningsih, I., Krisch, S., Lodeiro, P., Reichart, G.-J., Achterberg, E.P., Gledhill, M., Middag, R., Gerringa, L.J.A., 2020. Natural Fe-binding organic ligands in Fram Strait and over the northeast Greenland shelf. Mar. Chem. 224, 103815.

Arrigo, K.R., van Dijken, G.L., 2003. Phytoplankton dynamics within 37 Antarctic coastal polynya systems. J. Geophys. Res. Oceans 108, 3271.

Arrigo, K.R., van Dijken, G.L., Bushinsky, S., 2008. Primary production in the Southern Ocean, 1997–2006. J. Geophys. Res. Oceans 113, C08004.

Arrigo, K.R., Lowry, K.E., van Dijken, G.L., 2012. Annual changes in sea ice and phytoplankton in polynyas of the Amundsen Sea, Antarctica. Deep Sea Res. Part II 71–76, 5–15.

Beard, B.L., Johnson, C.M., 2004. Fe isotope variations in the modern and ancient Earth and other planetary bodies. Rev. Mineral. Geochem. 55, 319–357.

Beard, B.L., Johnson, C.M., Skulan, J.L., Nealson, K.H., Cox, L., Sun, H., 2003. Application of Fe isotopes to tracing the geochemical and biological cycling of Fe. Chem. Geol. 195, 87–117.

Bertrand, E.M., Saito, M.A., Rose, J.M., Riesselman, C.R., Lohan, M.C., Noble, A.E., Lee, P.A., DiTullio, G.R., 2007. Vitamin B12 and iron colimitation of phytoplankton growth in the Ross Sea. Limnol. Oceanogr. 52, 1079–1093.

Bertrand, E.M., McCrow, J.P., Moustafa, A., Zheng, H., McQuaid, J.B., Delmont, T.O., Post, A.F., Sipler, R.E., Spackeen, J.L., Xu, K., Bronk, D.A., Hutchins, D.A., Allen, A. E., 2015. Phytoplankton–bacterial interactions mediate micronutrient colimitation at the coastal Antarctic sea ice edge. Proc. Natl. Acad. Sci. 112, 9938–9943.

Boyd, P.W., Jickells, T., Law, C.S., Blain, S., Boyle, E.A., Buesseler, K.O., Coale, K.H., Cullen, J.J., de Baar, H.J.W., Follows, M., Harvey, M., Lancelot, C., Levasseur, M., Owens, N.P.J., Pollard, R., Rivkin, R.B., Sarmiento, J., Schoemann, V., Smetacek, V., Takeda, S., Tsuda, A., Turner, S., Watson, A.J., 2007. Mesoscale iron enrichment experiments 1993–2005: Synthesis and future directions. Science 315, 612–617.

Chen, X.-G., Krisch, S., Al-Hashem, A., Hopwood, M.J., Rutgers van der Loeff, M.M., Huhn, O., Lodeiro, P., Steffens, T., Achterberg, E.P., 2022. Dissolved, labile, and total particulate trace metal dynamics on the Northeast Greenland Shelf. Global Biogeochem. Cycles 36, e2022GB007528.

Conway, T.M., Hamilton, D.S., Shelley, R.U., Aguilar-Islas, A.M., Landing, W.M., Mahowald, N.M., John, S.G., 2019. Tracing and constraining anthropogenic aerosol iron fluxes to the North Atlantic Ocean using iron isotopes. Nat. Commun. 10, 2628.

Conway, T.M., John, S.G., 2014. Quantification of dissolved iron sources to the North Atlantic Ocean. Nature 511, 212–215.

Conway, T.M., Rosenberg, A.D., Adkins, J.F., John, S.G., 2013. A new method for precise determination of iron, zinc and cadmium stable isotope ratios in seawater by double-spike mass spectrometry. Anal. Chim. Acta 793, 44–52.

Conway, T.M., John, S.G., Lacan, F., 2016. Intercomparison of dissolved iron isotope profiles from reoccupation of three GEOTRACES stations in the Atlantic Ocean. Mar. Chem. 183, 50–61.
Crosby, H.A., Roden, E.E., Johnson, C.M., Beard, B.L., 2007. The mechanisms of iron isotope fractionation produced during dissimilatory Fe(III) reduction by Shewanella putrefaciens and Geobacter sulfurreducens. Geobiology 5, 169–189.
Cuvelier, M.L., Allen, A.E., Monier, A., McCrow, J.P., Messié, M., Tringe, S.G., Woyke, T., Welsh, R.M., Ishoey, T., Lee, J.-H., Binder, B.J., DuPont, C.L., Latasa, M., Guigand, C., Buck, K.R., Hilton, J., Thiagarajan, M., Caler, E., Read, B., Lasken, R.S., Chavez, F.P., Worden, A.Z., 2010. Targeted metagenomics and ecology of globally important uncultured eukaryotic phytoplankton. Proc. Natl. Acad. Sci. 107, 14679–14684.
Dauphas, N., John, S.G., Rouxel, O., 2017. Iron isotope systematics. Rev. Mineral. Geochem. 82, 415–510.
de Baar, H.J.W., de Jong, J.T.M., Bakker, D.C.E., Löscher, B.M., Veth, C., Bathmann, U., Smetacek, V., 1995. Importance of iron for plankton blooms and carbon dioxide drawdown in the Southern Ocean. Nature 373, 412–415.
de Baar, H.J.W., Timmermans, K.R., Laan, P., De Porto, H.H., Ober, S., Blom, J.J., Bakker, M.C., Schilling, J., Sarthou, G., Smit, M.G., Klunder, M., 2008. Titan: A new facility for ultraclean sampling of trace elements and isotopes in the deep oceans in the international Geotraces program. Mar. Chem. 111, 4–21.
de Jong, J., Schoemann, V., Lannuzel, D., Croot, P., de Baar, H., Tison, J.-L., 2012. Natural iron fertilization of the Atlantic sector of the Southern Ocean by continental shelf sources of the Antarctic Peninsula. J. Geophys. Res. Biogeo. 117, G01029.
Dideriksen, K., Baker, J.A., Stipp, S.L.S., 2008. Equilibrium Fe isotope fractionation between inorganic aqueous Fe(III) and the siderophore complex, Fe(III)-desferrioxamine B. Earth Planet. Sci. Lett. 269, 280–290.
Ellwood, M.J., Hutchins, D.A., Lohan, M.C., Milne, A., Nasemann, P., Nodder, S.D., Sander, S.G., Strzepek, R., Wilhelm, S.W., Boyd, P.W., 2015. Iron stable isotopes track pelagic iron cycling during a subtropical phytoplankton bloom. Proc. Natl. Acad. Sci. 112, E15–E20.
Ellwood, M.J., Strzepek, R.F., Strutton, P.G., Trull, T.W., Fourquez, M., Boyd, P.W., 2020. Distinct iron cycling in a Southern Ocean eddy. Nat. Commun. 11, 825.
Endo, H., Ogata, H., Suzuki, K., 2018. Contrasting biogeography and diversity patterns between diatoms and haptophytes in the central Pacific Ocean. Sci. Rep. 8, 10916.
Fitzsimmons, J.N., Conway, T.M., 2023. Novel Insights into Marine Iron Biogeochemistry from Iron Isotopes. Ann. Rev. Mar. Sci. 15, 383–406.
Fitzsimmons, J.N., John, S.G., Marsay, C.M., Hoffman, C.L., Nicholas, S.L., Toner, B.M., German, C.R., Sherrell, R.M., 2017. Iron persistence in a distal hydrothermal plume supported by dissolved–particulate exchange. Nat. Geosci. 10, 195–201.
Gerringa, L.J.A., Alderkamp, A.-C., Laan, P., Thuróczy, C.-E., De Baar, H.J.W., Mills, M. M., van Dijken, G.L., Haren, H., v. and Arrigo K. R., 2012. Iron from melting glaciers fuels the phytoplankton blooms in Amundsen Sea (Southern Ocean): Iron biogeochemistry. Deep Sea Res. Part II 71–76, 16–31.
Gerringa, L.J.A., Alderkamp, A.-C., van Dijken, G., Laan, P., Middag, R., Arrigo, K.R., 2020a. Dissolved trace metals in the Ross Sea. Front. Mar. Sci. 7, 874.
Gerringa, L.J.A., Alderkamp, A.-C., Laan, P., Thuróczy, C.-E., De Baar, H.J.W., Mills, M. M., van Dijken, G.L., Haren, H.V., Arrigo, K.R., 2020b. Corrigendum to "Iron from melting glaciers fuels the phytoplankton blooms in Amundsen Sea (Southern Ocean): iron biogeochemistry" (Gerringa et al., 2012). Deep Sea Res. Part II: Top. Stud. Oceanogr. 177, 104843.
Girton, J.B., Christianson, K., Dunlap, J., Dutrieux, P., Gobat, J., Lee, C., Rainville, L., 2019. Buoyancy-adjusting profiling floats for exploration of heat transport, melt rates, and mixing in the ocean cavities under floating ice shelves. OCEANS 2019 MTS/IEEE SEATTLE.
Gourmelen, N., Goldberg, D.N., Snow, K., Henley, S.F., Bingham, R.G., Kimura, S., Hogg, A.E., Shepherd, A., Mouginot, J., Lenaerts, J.T.M., Ligtenberg, S.R.M., van de Berg, W.J., 2017. Channelized melting drives thinning under a rapidly melting Antarctic Ice Shelf. Geophys. Res. Lett. 44, 9796–9804.
Halse, G.R., Syvertsen, E.E., 1996. Chapter 2 – Marine Diatoms. In: Tomas, C.R. (Ed.), Identifying Marine Diatoms and Dinoflagellates. Academic Press, San Diego, pp. 5–385.
Hatta, M., Measures, C.I., Selph, K.E., Zhou, M., Hiscock, W.T., 2013. Iron fluxes from the shelf regions near the South Shetland Islands in the Drake Passage during the austral-winter 2006. Deep Sea Res. Part II 90, 89–101.
Henkel, S., Kasten, S., Hartmann, J.F., Silva-Busso, A., Staubwasser, M., 2018. Iron cycling and stable Fe isotope fractionation in Antarctic shelf sediments, King George Island. Geochim. Cosmochim. Acta 237, 320–338.
Homoky, W.B., Severmann, S., Mills, R.A., Statham, P.J., Fones, G.R., 2009. Pore-fluid Fe isotopes reflect the extent of benthic Fe redox recycling: Evidence from continental shelf and deep-sea sediments. Geology 37, 751–754.
Homoky, W.B., John, S.G., Conway, T.M., Mills, R.A., 2013. Distinct iron isotopic signatures and supply from marine sediment dissolution. Nat. Commun. 4, 2143.
Homoky, W.B., Conway, T.M., John, S.G., König, D., Deng, F., Tagliabue, A., Mills, R.A., 2021. Iron colloids dominate sedimentary supply to the ocean interior. Proc. Natl. Acad. Sci. 118, e2016078118.
Hunt, H.R., Summers, B.A., Sieber, M., Krisch, S., Al-Hashem, A., Hopwood, M., Achterberg, E.P., Conway, T.M., 2022. Distinguishing the influence of sediments, the Congo River, and water-mass mixing on the distribution of iron and its isotopes in the Southeast Atlantic Ocean. Mar. Chem. 247, 104181.
Hutchins, D.A., Franck, V.M., Brzezinski, M.A., Bruland, K.W., 1999. Inducing phytoplankton iron limitation in iron-replete coastal waters with a strong chelating ligand. Limnol. Oceanogr. 44, 1009–1018.
Ilina, S.M., Poitrasson, F., Lapitskiy, S.A., Alekhin, Y.V., Viers, J., Pokrovsky, O.S., 2013. Extreme iron isotope fractionation between colloids and particles of boreal and temperate organic-rich waters. Geochim. Cosmochim. Acta 101, 96–111.
Jacobs, S.S., Hellmer, H.H., Jenkins, A., 1996. Antarctic Ice Sheet melting in the southeast Pacific. Geophys. Res. Lett. 23, 957–960.
Jacobs, S.S., Jenkins, A., Giulivi, C.F., Dutrieux, P., 2011. Stronger ocean circulation and increased melting under Pine Island Glacier ice shelf. Nat. Geosci. 4, 519–523.
Jeandel, C., 2016. Overview of the mechanisms that could explain the 'Boundary Exchange' at the land–ocean contact. Philos. Trans. R. Soc. A Math. Phys. Eng. Sci. 374, 20150287.
Jenkins, A., Dutrieux, P., Jacobs, S.S., McPhail, S.D., Perrett, J.R., Webb, A.T., White, D., 2010. Observations beneath Pine Island Glacier in West Antarctica and implications for its retreat. Nat. Geosci. 3, 468–472.
Jensen, L.T., Morton, P., Twining, B.S., Heller, M.I., Hatta, M., Measures, C.I., John, S., Zhang, R., Pinedo-Gonzalez, P., Sherrell, R.M., Fitzsimmons, J.N., 2020. A comparison of marine Fe and Mn cycling: U.S. GEOTRACES GN01 Western Arctic case study. Geochim. Cosmochim. Acta 288, 138–160.
John, S.G., Adkins, J., 2012. The vertical distribution of iron stable isotopes in the North Atlantic near Bermuda. Global Biogeochem. Cycles 26, GB2034.
John, S.G., Mendez, J., Moffett, J., Adkins, J., 2012. The flux of iron and iron isotopes from San Pedro Basin sediments. Geochim. Cosmochim. Acta 93, 14–29.
Johnson, C.M., Beard, B.L., Roden, E.E., 2008. The Iron Isotope Fingerprints of Redox and Biogeochemical Cycling in Modern and Ancient Earth. Annu. Rev. Earth Planet. Sci. 36, 457–493.
Johnson, C., Beard, B., Weyer, S., 2020. High-Temperature Fe Isotope Geochemistry. In: Iron Geochemistry: An Isotopic Perspective. Springer, Cham, pp. 85–147.
Jordan, T.A., Porter, D., Tinto, K., Millan, R., Muto, A., Hogan, K., Larter, R.D., Graham, A.G.C., Paden, J.D., 2020. New gravity-derived bathymetry for the Thwaites, Crosson, and Dotson ice shelves revealing two ice shelf populations. Cryosphere 14, 2869–2882.
Kim, S.-H., Choi, A., Jin, Y.E., Lee, S., Hyun, J.-H., 2016. Low benthic respiration and nutrient flux at the highly productive Amundsen Sea Polynya, Antarctica. Deep Sea Res. Part II 123, 92–101.
Kim, T.-W., Yang, H.W., Dutrieux, P., Wåhlin, A.K., Jenkins, A., Kim, Y.G., Ha, H.K., Kim, C.-S., Cho, K.-H., Park, T., Park, J., Lee, S., Cho, Y.-K., 2021. Interannual variation of modified circumpolar deep water in the Dotson-Getz Trough, West Antarctica. J. Geophys. Res.: Oceans 126, e2021JC017491.
Klar, J.K., Schlosser, C., Milton, J.A., Woodward, E.M.S., Lacan, F., Parkinson, I.J., Achterberg, E.P., James, R.H., 2018. Sources of dissolved iron to oxygen minimum zone waters on the Senegalese continental margin in the tropical North Atlantic Ocean: Insights from iron isotopes. Geochim. Cosmochim. Acta 236, 60–78.
Klunder, M.B., Laan, P., Middag, R., De Baar, H.J.W., van Ooijen, J.C., 2011. Dissolved iron in the Southern Ocean (Atlantic sector). Deep Sea Res. Part II 58, 2678–2694.
Klunder, M.B., Laan, P., De Baar, H.J.W., Middag, R., Neven, I., Van Ooijen, J., 2014. Dissolved Fe across the Weddell Sea and Drake Passage: impact of DFe on nutrient uptake. Biogeosciences 11, 651–669.
Krisch, S., Hopwood, M.J., Schaffer, J., Al-Hashem, A., Höfer, J., Rutgers van der Loeff, M.M., Conway, T.M., Summers, B.A., Lodeiro, P., Ardiningsih, I., Steffens, T., Achterberg, E.P., 2021. The 79°N Glacier cavity modulates subglacial iron export to the NE Greenland Shelf. Nat. Commun. 12, 3030.
Kurisu, M., Takahashi, Y., Iizuka, T., Uematsu, M., 2016a. Very low isotope ratio of iron in fine aerosols related to its contribution to the surface ocean. J. Geophys. Res.: Atmos. 121, 11119–111136.
Kurisu, M., Sakata, K., Miyamoto, C., Takaku, Y., Iizuka, T., Takahashi, Y., 2016b. Variation of iron isotope ratios in anthropogenic materials emitted through combustion processes. Chem. Lett. 45, 970–972.
Kurisu, M., Sakata, K., Uematsu, M., Ito, A., Takahashi, Y., 2021. Contribution of combustion Fe in marine aerosols over the northwestern Pacific estimated by Fe stable isotope ratios. Atmos. Chem. Phys. 21, 16027–16050.
Lacan, F., Jeandel, C., 2005. Neodymium isotopes as a new tool for quantifying exchange fluxes at the continent–ocean interface. Earth Planet. Sci. Lett. 232, 245–257.
Lacan, F., Artigue, L., Klar, J.K., Pradoux, C., Chmeleff, J., Freydier, R., 2021. Interferences and matrix effects on iron isotopic composition measurements by ^{57}Fe-^{58}Fe double-spike multi-collector inductively coupled plasma mass spectrometry; the importance of calcium and aluminum interferences. Front. Environ. Chem. 2, 692025.
Litchman, E., Klausmeier, C.A., Schofield, O.M., Falkowski, P.G., 2007. The role of functional traits and trade-offs in structuring phytoplankton communities: scaling from cellular to ecosystem level. Ecol. Lett. 10, 1170–1181.
Lough, A.J.M., Klar, J.K., Homoky, W.B., Comer-Warner, S.A., Milton, J.A., Connelly, D. P., James, R.H., Mills, R.A., 2017. Opposing authigenic controls on the isotopic signature of dissolved iron in hydrothermal plumes. Geochim. Cosmochim. Acta 202, 1–20.
Mankoff, K.D., Jacobs, S.S., Tulaczyk, S.M., Stammerjohn, S.E., 2012. The role of Pine Island Glacier ice shelf basal channels in deep-water upwelling, polynyas and ocean circulation in Pine Island Bay, Antarctica. Ann. Glaciol. 53, 123–128.
Margalef, R., 1978. Life-forms of phytoplankton as survival alternatives in an unstable environment. Oceanol. Acta 1, 493–509.
Marsay, C.M., Lam, P.J., Heller, M.I., Lee, J.-M., John, S.G., 2018. Distribution and isotopic signature of ligand-leachable particulate iron along the GEOTRACES GP16 East Pacific Zonal Transect. Mar. Chem. 201, 198–211.
Martin, J.H., Fitzwater, S.E., Gordon, R.M., 1990. Iron deficiency limits phytoplankton growth in Antarctic waters. Global Biogeochem. Cycles 4, 5–12.
Masquelier, S., Foulon, E., Jouenne, F., Ferréol, M., Brussaard, C.P.D., Vaulot, D., 2011. Distribution of eukaryotic plankton in the English Channel and the North Sea in summer. J. Sea Res. 66, 111–122.
Measures, C.I., Brown, M.T., Selph, K.E., Apprill, A., Zhou, M., Hatta, M., Hiscock, W.T., 2013. The influence of shelf processes in delivering dissolved iron to the HNLC

waters of the Drake Passage, Antarctica. Deep-Sea Res. Part II: Top. Stud. Oceanogr. 90, 77–88.
Middag, R., de Baar, H.J.W., Bruland, K.W., 2019. The relationships between dissolved zinc and major nutrients phosphate and silicate along the GEOTRACES GA02 transect in the West Atlantic Ocean. Global Biogeochem. Cycles 33, 63–84.
Mikucki, J.A., Foreman, C.M., Sattler, B., Berry, L.W., Priscu, J.C., 2004. Geomicrobiology of blood falls: An iron-rich saline discharge at the terminus of the Taylor Glacier, Antarctica. Aquat. Geochem. 10, 199–220.
Miles, T., Lee, S.H., Wåhlin, A., Ha, H.K., Kim, T.W., Assmann, K.M., Schofield, O., 2016. Glider observations of the Dotson Ice Shelf outflow. Deep Sea Res. Part II 123, 16–29.
Morel, F.M.M., Price, N.M., 2003. The biogeochemical cycles of trace metals in the oceans. Science 300, 944.
Morel, F.M.M., Kustka, A.B., Shaked, Y., 2008. The role of unchelated Fe in the iron nutrition of phytoplankton. Limnol. Oceanogr. 53, 400–404.
Morgan, J.L.L., Wasylenki, L.E., Nuester, J., Anbar, A.D., 2010. Fe isotope fractionation during equilibration of Fe–organic complexes. Environ. Sci. Technol. 44, 6095–6101.
Mosby, H., 1936. Part XIII. Physical oceanography. Geogr. Ann. 18, 20–29.
Mulholland, D.S., Poitrasson, F., Shirokova, L.S., González, A.G., Pokrovsky, O.S., Boaventura, G.R., Vieira, L.C., 2015. Iron isotope fractionation during Fe(II) and Fe (III) adsorption on cyanobacteria. Chem. Geol. 400, 24–33.
Paolo, F.S., Fricker, H.A., Padman, L., 2015. Volume loss from Antarctic ice shelves is accelerating. Science 348, 327–331.
Park, J., Kuzminov, F.I., Bailleul, B., Yang, E.J., Lee, S., Falkowski, P.G., Gorbunov, M.Y., 2017. Light availability rather than Fe controls the magnitude of massive phytoplankton bloom in the Amundsen Sea polynyas, Antarctica. Limnol. Oceanogr. 62, 2260–2276.
Parry, G.D., 1981. The meanings of r- and K-selection. Oecologia 48, 260–264.
Planquette, H., Sherrell, R.M., Stammerjohn, S., Field, M.P., 2013. Particulate iron delivery to the water column of the Amundsen Sea, Antarctica. Mar. Chem. 153, 15–30.
Radic, A., Lacan, F., Murray, J.W., 2011. Iron isotopes in the seawater of the equatorial Pacific Ocean: New constraints for the oceanic iron cycle. Earth Planet. Sci. Lett. 306, 1–10.
Raiswell, R., Tranter, M., Benning, L.G., Siegert, M., De'ath, R., Huybrechts, P., Payne, T., 2006. Contributions from glacially derived sediment to the global iron (oxyhydr) oxide cycle: Implications for iron delivery to the oceans. Geochim. Cosmochim. Acta 70, 2765–2780.
Randall-Goodwin, Meredith, M.P., Jenkins, A.L., Yager, P., Sherrell, R.M., Abrahamsen, E.P., Guerrero, R., Yuan, X., Mortlock, R.A., Gavahan, K., Alderkamp, A.-C., Ducklow, H., Robertson, R., Stammerjohn, S.E., 2015. Freshwater distributions and water mass structure in the Amundsen Sea Polynya region, Antarctica. Elementa: Sci. Anthropocene 3, 000065.
Rignot, E., Bamber, J.L., van den Broeke, M.R., Davis, C., Li, Y., van de Berg, W.J., van Meijgaard, E., 2008. Recent Antarctic ice mass loss from radar interferometry and regional climate modelling. Nat. Geosci. 1, 106–110.
Rignot, E., Mouginot, J., Scheuchl, B., van den Broeke, M., van Wessem, M.J., Morlighem, M., 2019. Four decades of Antarctic Ice Sheet mass balance from 1979–2017. Proc. Natl. Acad. Sci. 116, 1095–1103.
Rijkenberg, M.J.A., de Baar, H.J.W., Bakker, K., Gerringa, L.J.A., Keijzer, E., Laan, M., Laan, P., Middag, R., Ober, S., van Ooijen, J., Ossebaar, S., van Weerlee, E.M., Smit, M.G., 2015. "PRISTINE", a new high volume sampler for ultraclean sampling of trace metals and isotopes. Mar. Chem. 177, 501–509.
Rouxel, O.J., Auro, M., 2010. Iron isotope variations in coastal seawater determined by multicollector ICP-MS. Geostand. Geoanal. Res. 34, 135–144.
Sarmiento, J.L., Gruber, N., Brzezinski, M.A., Dunne, J.P., 2004. High-latitude controls of thermocline nutrients and low latitude biological productivity. Nature 427, 56–60.
Schaffer, J., Kanzow, T., von Appen, W.-J., von Albedyll, L., Arndt, J.E., Roberts, D.H., 2020. Bathymetry constrains ocean heat supply to Greenland's largest glacier tongue. Nat. Geosci. 13, 227–231.
Schlitzer, R., 2020. Ocean Data View.
Schroth, A.W., Crusius, J., Chever, F., Bostick, B.C., Rouxel, O.J., 2011. Glacial influence on the geochemistry of riverine iron fluxes to the Gulf of Alaska and effects of deglaciation. Geophys. Res. Lett. 38, L16605.
Sedwick, P.N., DiTullio, G.R., 1997. Regulation of algal blooms in Antarctic Shelf Waters by the release of iron from melting sea ice. Geophys. Res. Lett. 24, 2515–2518.
Sedwick, P.N., Bowie, A.R., Trull, T.W., 2008. Dissolved iron in the Australian sector of the Southern Ocean (CLIVAR SR3 section): Meridional and seasonal trends. Deep Sea Res. Part I 55, 911–925.
Severmann, S., Johnson, C.M., Beard, B.L., McManus, J., 2006. The effect of early diagenesis on the Fe isotope compositions of porewaters and authigenic minerals in continental margin sediments. Geochim. Cosmochim. Acta 70, 2006–2022.
Severmann, S., McManus, J., Berelson, W.M., Hammond, D.E., 2010. The continental shelf benthic iron flux and its isotope composition. Geochim. Cosmochim. Acta 74, 3984–4004.
Sherrell, R.M., Lagerström, M.E., Forsch, K.O., Stammerjohn, S.E., Yager, P.L., 2015. Dynamics of dissolved iron and other bioactive trace metals (Mn, Ni, Cu, Zn) in the Amundsen Sea Polynya, Antarctica. Elementa: Sci. Anthropocene 3, 000071.
Sieber, M., Conway, T.M., de Souza, G.F., Hassler, C.S., Ellwood, M.J., Vance, D., 2021. Isotopic fingerprinting of biogeochemical processes and iron sources in the iron-limited surface Southern Ocean. Earth Planet. Sci. Lett. 567, 116967.
Siebert, C., Nägler, T.F., Kramers, J.D., 2001. Determination of molybdenum isotope fractionation by double-spike multicollector inductively coupled plasma mass spectrometry. Geochem. Geophys. Geosyst. 2, 1032.
Stevenson, E.I., Fantle, M.S., Das, S.B., Williams, H.M., Aciego, S.M., 2017. The iron isotopic composition of subglacial streams draining the Greenland ice sheet. Geochim. Cosmochim. Acta 213, 237–254.
St-Laurent, P., Yager, P.L., Sherrell, R.M., Oliver, H., Dinniman, M.S., Stammerjohn, S.E., 2019. Modeling the seasonal cycle of iron and carbon fluxes in the Amundsen Sea Polynya, Antarctica. J. Geophys. Res. Oceans 124, 1544–1565.
Sun, M., Archer, C., Vance, D., 2021. New methods for the chemical isolation and stable isotope measurement of multiple transition metals, with application to the earth sciences. Geostand. Geoanal. Res. 45, 643–658.
Tagliabue, A., Mtshali, T., Aumont, O., Bowie, A.R., Klunder, M.B., Roychoudhury, A.N., Swart, S., 2012. A global compilation of dissolved iron measurements: Focus on distributions and processes in the Southern Ocean. Biogeosciences 9, 2333–2349.
Tagliabue, A., Sallée, J.-B., Bowie, A.R., Lévy, M., Swart, S., Boyd, P.W., 2014. Surface-water iron supplies in the Southern Ocean sustained by deep winter mixing. Nat. Geosci. 7, 314–320.
Thuróczy, C.-E., Alderkamp, A.-C., Laan, P., Gerringa, L.J.A., Mills, M.M., Van Dijken, G. L., De Baar, H.J.W., Arrigo, K.R., 2012. Key role of organic complexation of iron in sustaining phytoplankton blooms in the Pine Island and Amundsen Polynyas (Southern Ocean). Deep Sea Res. Part II 71–76, 49–60.
Tian, H.-A., van Manen, M., Wille, F., Jung, J., Lee, S., Kim, T.-W., Aoki, S., Eich, C., Brussaard, C.P.D., Reichart, G.-J., Conway, T.M., Middag, R., 2023. The biogeochemistry of zinc and cadmium in the Amundsen Sea, coastal Antarctica. Mar. Chem. 249, 104223.
van Manen, M., Tian, H.-A., Wille, F., Jung, J., Lee, Y., Lee, S.H., Kim, T.-W., Aoki, S., Eich, C., Brussaard, C., Reichart, G.-J., Gerringa, L., Conway, T.M., Middag, R., 2022. The role of the Dotson Ice Shelf and circumpolar deepwater as driver and source of dissolved and particulate iron and manganese in the Amundsen Sea polynya, Southern Ocean. Mar. Chem. 246, 104161.
Vaughan, D.G., 2008. West Antarctic Ice Sheet collapse – the fall and rise of a paradigm. Clim. Change 91, 65–79.
Wåhlin, A.K., Yuan, X., Björk, G., Nohr, C., 2010. Inflow of warm circumpolar deep water in the Central Amundsen Shelf. J. Phys. Oceanogr. 40, 1427–1434.
Walker, D.P., Brandon, M.A., Jenkins, A., Allen, J.T., Dowdeswell, J.A., Evans, J., 2007. Oceanic heat transport onto the Amundsen Sea shelf through a submarine glacial trough. Geophys. Res. Lett. 34, L02602.
Wang, W., Lough, A., Lohan, M.C., Connelly, D.P., Cooper, M., Milton, J.A., Chavagnac, V., Castillo, A., James, R.H., 2021. Behavior of iron isotopes in hydrothermal systems: Beebe and Von Damm vent fields on the Mid-Cayman ultraslow-spreading ridge. Earth Planet. Sci. Lett. 575, 117200.
Yager, P.L., Sherrell, R.M., Stammerjohn, S.E., Alderkamp, A.-C., Schofield, O., Abrahamsen, E.P., Arrigo, K.R., Bertilsson, S., Garay, D.L., Guerrero, R., Lowry, K.E., Moksnes, P.-O., Ndungu, K., Post, A.F., Randall-Goodwin, E., Riemann, L., Severmann, S., Thatje, S., Van Dijken, G.L., Wilson, S., 2012. ASPIRE: The Amundsen Sea polynya international research expedition. Oceanography 25, 40–53.
Yager, P., Sherrell, R., Stammerjohn, S., Ducklow, H., Schofield, O., Ingall, E., Wilson, S., Lowry, K., Williams, C., Riemann, L., Bertilsson, S., Alderkamp, A.-C., Dinasquet, J., Logares, R., Richert, I., Sipler, R., Melara, A., Mu, L., Newstead, R., Post, A., Swalethorp, R., van Dijken, G.L., 2016. A carbon budget for the Amundsen Sea Polynya, Antarctica: Estimating net community production and export in a highly productive polar ecosystem. Elem. Sci. Anth. 4, 000140.
Yang, H., Krebs-Kanzow, U., Kleiner, T., Sidorenko, D., Rodehacke, C.B., Shi, X., Gierz, P., Niu, L., Gowan, E.J., Hinck, S., Liu, X., Stap, L.B., Lohmann, G., 2022. Impact of paleoclimate on present and future evolution of the Greenland Ice Sheet. PLoS One 17, e0259816.
Zhang, R., Jensen, L., Fitzsimmons, J., Sherrell, R.M., Lam, P., Xiang, Y., John, S., 2021. Iron isotope biogeochemical cycling in the western Arctic Ocean. Global Biogeochem. Cycles 35, e2021GB006977.
Zhang, F., Zhu, X., Yan, B., Kendall, B., Peng, X., Li, J., Algeo, T.J., Romaniello, S., 2015. Oxygenation of a Cryogenian ocean (Nanhua Basin, South China) revealed by pyrite Fe isotope compositions. Earth Planet. Sci. Lett. 429, 11–19.